

Citation:

Bucha B, Hirt C, Kuhn M (2019) Cap integration in spectral gravity forward modelling up to the full gravity tensor, *Journal of Geodesy*, DOI: 10.1007/s00190-019-01277-3

Note: This is a preprint (author's own manuscript that has not been peer reviewed) of an article accepted for publication in *Journal of Geodesy*. The final authenticated version will soon be available online at the website of *Journal of Geodesy*.

Cap integration in spectral gravity forward modelling up to the full gravity tensor

Blažej Bucha · Christian Hirt · Michael Kuhn

Received: / Accepted:

Abstract Cap-modified spectral gravity forward modelling is extended in this paper to the full gravity vector and tensor expressed in the local north-oriented reference frame. This is achieved by introducing three new groups of altitude-dependent Molodensky's truncation coefficients. These are given by closed-form and infinite spectral relations that are generalized for i) an arbitrary harmonic degree, ii) an arbitrary topography power, iii) an arbitrary radial derivative, iv) any radius larger than the radius of the reference sphere, and v) for both near- and far-zone gravity effects. Thanks to the generalization for an arbitrary radial derivative, the cap-modified technique can efficiently be combined with the gradient approach for harmonic synthesis on irregular surfaces. In a numerical study, we exemplarily apply the new technique by forward modelling Earth's degree-2159 topography up to degree 21,590, employing 30 topography powers. The experiment shows that near- and far-zone gravity effects can be synthesized on the topography with an accuracy (RMS) of $0.005 - 0.03 \text{ m}^2 \text{ s}^{-2}$ (potential), $0.8 - 20 \mu\text{Gal}$ (gravity vector) and $0.1 \text{ mE} - 1 \text{ E}$ (gravity tensor). The numerical experiment also shows that the divergence effect of spherical harmonics comes into play around degree 10,795 when evaluating the series on the Earth's surface.

Blažej Bucha

Department of Theoretical Geodesy, Slovak University of Technology in Bratislava, Radlinského 11, 81005 Bratislava, Slovak Republic
E-mail: blazej.bucha@stuba.sk

Christian Hirt

Institute for Astronomical and Physical Geodesy & Institute for Advanced Study, Technische Universität München, Arcisstr 21, 80333 München, Germany
E-mail: c.hirt@tum.de

Michael Kuhn

School of Earth and Planetary Sciences & Western Australian Geodesy Group, Curtin University, GPO Box U1987, Perth, WA 6845, Australia
E-mail: m.kuhn@curtin.edu.au

The difficult-to-compute truncation coefficients that are employed in the study are made freely available at <http://edisk.cvt.stuba.sk/~xbuchab/> and are accompanied by Matlab-based routines to evaluate them. Enclosed is also a Matlab-based package to perform ultra-high-degree surface spherical harmonic analysis, a step of central importance in spectral gravity forward modelling techniques.

Keywords Spectral gravity forward modelling · Topographic potential · Spherical harmonics · Molodensky's truncation coefficients · Divergence effect

1 Introduction

Spectral gravity forward modelling (e.g., Rummel et al, 1988; Martinec and Pěč, 1989; Balmino, 1994; Wieczorek and Phillips, 1998; Hirt and Kuhn, 2014) is a technique to deliver the gravitational field induced by a topographic mass distribution using spherical (or other) harmonics. Its recent applications include computations of Bouguer anomalies (Balmino et al, 2012; Hirt et al, 2016), quasigeoid-to-geoid separation (Tenzer et al, 2016), studying the gravity effect due to the Earth's flattening (Wang and Yang, 2013; Rexer et al, 2016), investigation of the convergence/divergence behaviour of spherical harmonics on planetary surfaces (Hirt et al, 2016; Hirt and Kuhn, 2017; Bucha et al, 2019b) or the exploration and mitigation of the harmonic correction issue and the spectral filter problem of residual terrain modelling (RTM, Rexer et al, 2018; Hirt et al, 2019).

Common to these studies is that they forward model topographic masses over the entire globe (global integration). While this is required by potential theory in most instances, practical evaluations may necessitate a restriction of the integration domain, for instance, to masses inside/outside a spherical cap centred at the evaluation point. The resulting

cap integration then delivers near- or far-zone gravity effects, respectively. Perhaps most frequently, the restriction is done in order to lower the computational burden associated with the evaluation of the Newton integral in the spatial domain. To enable the inside- and outside-cap integration also for the spectral domain, Bucha et al (2019a) modified spectral gravity forward modelling by introducing Molodensky's truncation coefficients (Molodensky et al, 1962). In this paper, this technique is denoted as cap-modified spectral gravity forward modelling or simply as cap-modified spectral technique. Currently, it enables the computation of an arbitrary radial derivative of the gravitational potential at any point above the field-generating masses, provided that the spherical harmonic series converges which holds true at least at points above the limit sphere encompassing all gravitating masses (the sphere of convergence; e.g., Hotine 1969).

The cap-modified spectral technique is particularly suited when a specific spectral band of near- and/or far-zone gravity effects is sought. A prominent example is the RTM technique, in which gravity effects due to the reference (smooth) topography need to be band-limited in the spectral domain and at the same time spatially restricted to inside-cap masses (cf. Bucha et al, 2019a). Other applications include an efficient development of high-resolution global gravity maps or investigations of the near- and/or far-zone gravity spectra (*ibid.*).

In this paper, we extend the cap-modified spectral technique to the full gravity vector and tensor expressed in the local north-oriented reference frame (LNOF). In addition, we also provide means to evaluate an arbitrary radial derivative of these quantities, thereby enabling to compute, for instance, 6 out of 10 components of the third-order gravitational tensor (after considering its symmetry). The present study thus extends cap-modified spectral gravity forward modelling to the large palette of commonly used gravity field quantities such as the height anomalies, the gravity, the deflections of the vertical or the gravity tensor.

In a numerical case study, we apply the new technique to gravity effects implied by the Earth's degree-2159 topography and validate the results against an independent spatial-domain Newtonian integration that provides accurate reference values. In particular, we model 10 quantities: the gravitational potential, the three elements of the gravitational vector and the six elements of the gravitational tensor. All of them are evaluated up to degree 21,590 relying on 30 powers of the topography. As an additional outcome of the experiment, these rather advanced settings allow us to provide further insights into the divergence effect of spherical harmonics on planetary surfaces (e.g., Jekeli, 1981, 1983; Moritz, 1980; Hu and Jekeli, 2015; Hirt et al, 2016; Hirt and Kuhn, 2017; Rexer, 2017; Bucha et al, 2019b; Chen et al, 2019).

The paper is organized as follows. After a brief recapitulation of the basic principles of global and cap-modified spectral gravity forward modelling in Section 2, we proceed with extending the cap-modified technique up to the second-order derivatives of the gravitational potential in Section 3. The derivations (Appendices A to C) are then validated in Section 4 in a controlled environment using synthetic gravity field implied by the Earth's degree-2159 topography. In Section 5, we summarize the main conclusions of the paper and discuss topics that may be relevant to future investigations. The full statistical information from our validation experiments and selected visualisations are provided in the Electronic Supplementary Materials (ESM) to this paper.

2 Global and cap-modified spectral gravity forward modelling

Let the shape of the gravitating topographic masses be given by topographic heights \hat{H} measured in the radial direction from a reference sphere Ω having the radius R (spherical arrangement of the topographic masses). Next, the topographic heights \hat{H} are transformed into a dimensionless topographic height function

$$H(\varphi, \lambda) = \frac{\hat{H}(\varphi, \lambda)}{R}, \quad (1)$$

which can be approximated by a finite surface spherical harmonic expansion

$$H(\varphi, \lambda) = \sum_{n=0}^{n_{\max}} \sum_{m=-n}^n \bar{H}_{nm} \bar{Y}_{nm}(\varphi, \lambda). \quad (2)$$

Here, (φ, λ) are the spherical latitude and longitude, respectively, $\bar{Y}_{nm}(\varphi, \lambda)$ are the fully normalized spherical harmonic functions of degree n and order m (e.g., Heiskanen and Moritz, 1967), \bar{H}_{nm} are the spherical harmonic coefficients of the topographic height function and n_{\max} is the maximum degree of the expansion.

Assuming a constant mass density ρ , spectral gravity forward modelling approximates the implied gravitational potential V by a solid spherical harmonic expansion of the form (e.g., Balmino, 1994; Wieczorek and Phillips, 1998)

$$\begin{aligned} V(r, \varphi, \lambda) = & 2\pi G \rho R^2 \sum_{p=1}^{p_{\max}} \sum_{n=0}^{p \times n_{\max}} S_{np}(r) \\ & \times \sum_{m=-n}^n \bar{H}_{nmp} \bar{Y}_{nm}(\varphi, \lambda), \end{aligned} \quad (3)$$

where r is the spherical radius of the evaluation point, G is the gravitational constant, p is the integer power of the topography, \bar{H}_{nmp} are the fully normalized spherical harmonic

coefficients of the p th power of the topographic height function,

$$H^p(\varphi, \lambda) = \left(\frac{\hat{H}(\varphi, \lambda)}{R} \right)^p = \sum_{n=0}^{p \times n_{\max}} \sum_{m=-n}^n \bar{H}_{nmp} \bar{Y}_{nm}(\varphi, \lambda), \quad (4)$$

and, finally, the term $S_{np}(r)$ is given as

$$S_{np}(r) = \frac{2}{2n+1} \frac{\prod_{i=1}^p (n+4-i)}{p!(n+3)} \left(\frac{R}{r} \right)^{n+1}. \quad (5)$$

For the explanation of the maximum degree $p \times n_{\max}$ in Eq. (4), see, for instance, Freeden and Schneider (1998), Hirt and Kuhn (2014) or Bucha et al (2019a). Note that both n_{\max} and p_{\max} are generally infinite in case of real-world objects, but are truncated here for practical reasons. The convergence of the infinite series in Eq. (3) is guaranteed for evaluation points satisfying the condition $r > \max(R + \hat{H}(\varphi, \lambda))$. Otherwise, the infinite series may converge or diverge (e.g., Rummel et al, 1988; Wieczorek and Phillips, 1998; Balmino, 1994; Hirt and Kuhn, 2017; Bucha et al, 2019a,b).

The gravitational potential V from Eq. (3) is induced by topographic masses all around the globe. To restrict the integration from the whole sphere to a spherical cap, cap-modified gravity forward modelling introduced by Bucha et al (2019a) can be employed. With ψ_0 being the spherical radius of the cap, this leads to

$$V^j(r, \varphi, \lambda) = 2\pi G\rho R^2 \sum_{p=1}^{p_{\max}} \sum_{n=0}^{p \times n_{\max}} Q_{np}^j(r, \psi_0) \times \sum_{m=-n}^n \bar{H}_{nmp} \bar{Y}_{nm}(\varphi, \lambda), \quad (6)$$

where the variable $j = \{\text{'In'}, \text{'Out'}\}$ denotes either near-zone effects (inside-cap integration, $j = \text{'In'}$) or far-zone effects (outside-cap integration, $j = \text{'Out'}$) and the symbol $Q_{np}^j(r, \psi_0)$ stands for Molodensky's truncation coefficients, which are defined in Appendix A of Bucha et al (2019a). For the numerical evaluation of the $Q_{np}^j(r, \psi_0)$ coefficients and their radial derivatives, either infinite spectral relations or recurrence relations with a fixed number of terms can be used (cf. Appendices B, C and D of Bucha et al, 2019a). Needless to say, it holds that

$$V^{\text{In}}(r, \varphi, \lambda) + V^{\text{Out}}(r, \varphi, \lambda) = V(r, \varphi, \lambda). \quad (7)$$

3 Extension of cap-modified spectral gravity forward modelling up to the second-order potential derivatives in LNOF

Throughout the paper, the directional derivatives of the gravitational potential are expressed in LNOF, which is a right-handed orthogonal coordinate system, whose origin is at the

evaluation point $P(r, \varphi, \lambda)$ and its axes are defined as follows: the x -axis points to the north, the y -axis points to the west and the z -axis points radially outwards.

3.1 First-order potential derivatives in LNOF

Applying the gradient operator expressed in LNOF to Eq. (6), the gravitational vector induced by the near- and far-zone topographic masses is given as (Appendix A)

$$\mathbf{g}^j(r, \varphi, \lambda) = \nabla V^j(r, \varphi, \lambda) = \begin{bmatrix} V^x,j(r, \varphi, \lambda) \\ V^y,j(r, \varphi, \lambda) \\ V^z,j(r, \varphi, \lambda) \end{bmatrix}, \quad (8)$$

where

$$V^x,j(r, \varphi, \lambda) = -2\pi G\rho R^2 \sum_{p=1}^{p_{\max}} \sum_{n=1}^{p \times n_{\max}} Q_{np}^{1,1,j}(r, \psi_0) \times \sum_{m=-n}^n \bar{H}_{nmp} \frac{\partial \bar{Y}_{nm}(\varphi, \lambda)}{\partial \varphi}, \quad (9)$$

$$V^y,j(r, \varphi, \lambda) = \frac{2\pi G\rho R^2}{\cos \varphi} \sum_{p=1}^{p_{\max}} \sum_{n=1}^{p \times n_{\max}} Q_{np}^{1,1,j}(r, \psi_0) \times \sum_{m=-n}^n \bar{H}_{nmp} \frac{\partial \bar{Y}_{nm}(\varphi, \lambda)}{\partial \lambda} \quad (10)$$

and

$$V^z,j(r, \varphi, \lambda) = 2\pi G\rho R^2 \sum_{p=1}^{p_{\max}} \sum_{n=0}^{p \times n_{\max}} Q_{np}^{1,0,j}(r, \psi_0) \times \sum_{m=-n}^n \bar{H}_{nmp} \bar{Y}_{nm}(\varphi, \lambda). \quad (11)$$

The newly introduced truncation coefficients, $Q_{np}^{1,0,j}(r, \psi_0)$ and $Q_{np}^{1,1,j}(r, \psi_0)$, are defined in Eqs. (45) and (54) of Appendix A. The first superscript next to Q (here 1) indicates that the truncation coefficients relate to the first-order derivatives of the topographic potential and the second superscript (here either 0 or 1) stands for the order of the derivative with respect to the spherical distance ψ (cf. Eq. 38). The practical evaluation of these coefficients via infinite series and closed relations is discussed in Appendices A.1 and A.2, respectively. From (59) and (60), it follows that $Q_{np}^{1,0,j}(r, \psi_0)$ and $Q_{np}^{1,1,j}(r, \psi_0)$ are related to $Q_{np}^j(r, \psi_0)$ from Eq. (6). Worth noting is that two types of truncation coefficients are used to compute three elements the gravitational vector. Finally, Eqs. (9) and (10) are singular at the poles. As a remedy, the strategy by, for instance, Petrovskaya and Vershkov (2006) could be investigated to avoid the issue.

3.2 Second-order potential derivatives in LNOF

Continuing the differentiation in LNOF, the near- and far-zone effects on the gravitational tensor read (Appendix B)

$$\begin{aligned} \mathbf{V}^j(r, \varphi, \lambda) &= \nabla \otimes \nabla V^j(r, \varphi, \lambda) \\ &= \begin{bmatrix} V^{xx,j}(r, \varphi, \lambda) & V^{xy,j}(r, \varphi, \lambda) & V^{xz,j}(r, \varphi, \lambda) \\ V^{yx,j}(r, \varphi, \lambda) & V^{yy,j}(r, \varphi, \lambda) & V^{yz,j}(r, \varphi, \lambda) \\ V^{zx,j}(r, \varphi, \lambda) & V^{zy,j}(r, \varphi, \lambda) & V^{zz,j}(r, \varphi, \lambda) \end{bmatrix}, \end{aligned} \quad (12)$$

where

$$\begin{aligned} V^{xx,j}(r, \varphi, \lambda) &= V_1^{xx,j}(r, \varphi, \lambda) + V_2^{xx,j}(r, \varphi, \lambda) \\ &\quad + V_3^{xx,j}(r, \varphi, \lambda), \end{aligned} \quad (13)$$

$$\begin{aligned} V_1^{xx,j}(r, \varphi, \lambda) &= -\pi G \rho R^2 \sum_{p=1}^{p_{\max}} \sum_{n=0}^{p \times n_{\max}} Q_{np}^{2,0,j}(r, \psi_0) \\ &\quad \times \sum_{m=-n}^n \bar{H}_{nmp} \bar{Y}_{nm}(\varphi, \lambda), \end{aligned} \quad (14)$$

$$\begin{aligned} V_2^{xx,j}(r, \varphi, \lambda) &= 2\pi G \rho R^2 \sum_{p=1}^{p_{\max}} \sum_{n=2}^{p \times n_{\max}} n(n+1) Q_{np}^{2,2,j}(r, \psi_0) \\ &\quad \times \sum_{m=-n}^n \bar{H}_{nmp} \bar{Y}_{nm}(\varphi, \lambda), \end{aligned} \quad (15)$$

$$\begin{aligned} V_3^{xx,j}(r, \varphi, \lambda) &= 4\pi G \rho R^2 \sum_{p=1}^{p_{\max}} \sum_{n=2}^{p \times n_{\max}} Q_{np}^{2,2,j}(r, \psi_0) \\ &\quad \times \sum_{m=-n}^n \bar{H}_{nmp} \frac{\partial^2 \bar{Y}_{nm}(\varphi, \lambda)}{\partial \varphi^2}, \end{aligned} \quad (16)$$

$$V^{xy,j}(r, \varphi, \lambda) = V_1^{xy,j}(r, \varphi, \lambda) + V_2^{xy,j}(r, \varphi, \lambda), \quad (17)$$

$$\begin{aligned} V_1^{xy,j}(r, \varphi, \lambda) &= -\frac{4\pi G \rho R^2}{\cos \varphi} \tan \varphi \sum_{p=1}^{p_{\max}} \sum_{n=2}^{p \times n_{\max}} Q_{np}^{2,2,j}(r, \psi_0) \\ &\quad \times \sum_{m=-n}^n \bar{H}_{nmp} \frac{\partial \bar{Y}_{nm}(\varphi, \lambda)}{\partial \lambda}, \end{aligned} \quad (18)$$

$$\begin{aligned} V_2^{xy,j}(r, \varphi, \lambda) &= -\frac{4\pi G \rho R^2}{\cos \varphi} \sum_{p=1}^{p_{\max}} \sum_{n=2}^{p \times n_{\max}} Q_{np}^{2,2,j}(r, \psi_0) \\ &\quad \times \sum_{m=-n}^n \bar{H}_{nmp} \frac{\partial^2 \bar{Y}_{nm}(\varphi, \lambda)}{\partial \lambda \partial \varphi}, \end{aligned} \quad (19)$$

$$\begin{aligned} V^{xz,j}(r, \varphi, \lambda) &= 2\pi G \rho R^2 \sum_{p=1}^{p_{\max}} \sum_{n=1}^{p \times n_{\max}} Q_{np}^{2,1,j}(r, \psi_0) \\ &\quad \times \sum_{m=-n}^n \bar{H}_{nmp} \frac{\bar{Y}_{nm}(\varphi, \lambda)}{\partial \varphi}, \end{aligned} \quad (20)$$

$$\begin{aligned} V^{yy,j}(r, \varphi, \lambda) &= V_1^{xx,j}(r, \varphi, \lambda) - V_2^{xx,j}(r, \varphi, \lambda) \\ &\quad - V_3^{xx,j}(r, \varphi, \lambda), \end{aligned} \quad (21)$$

$$\begin{aligned} V^{yz,j}(r, \varphi, \lambda) &= -\frac{2\pi G \rho R^2}{\cos \varphi} \sum_{p=1}^{p_{\max}} \sum_{n=1}^{p \times n_{\max}} Q_{np}^{2,1,j}(r, \psi_0) \\ &\quad \times \sum_{m=-n}^n \bar{H}_{nmp} \frac{\partial \bar{Y}_{nm}(\varphi, \lambda)}{\partial \lambda}, \end{aligned} \quad (22)$$

$$V^{zz,j}(r, \varphi, \lambda) = -2V_1^{xx,j}(r, \varphi, \lambda). \quad (23)$$

Since the gravitational tensor is symmetric, it holds that $V^{xy}(r, \varphi, \lambda) = V^{yx}(r, \varphi, \lambda)$, etc. The truncation coefficients $Q_{np}^{2,0,j}(r, \psi_0)$, $Q_{np}^{2,1,j}(r, \psi_0)$ and $Q_{np}^{2,2,j}(r, \psi_0)$ are defined in Eqs. (78) and (85) and formulae suitable for their practical evaluation are discussed in Appendices B.1 and B.2. Note that only three groups of truncation coefficients enters the evaluation of six unique elements of the gravitational tensor. Similarly as in the previous section, these truncation coefficients are related to $Q_{np}^j(r, \psi_0)$ via Eqs. (90), (91) and (92), and singular expressions occur as well (Eqs. 16, 18, 19, 20, 22).

3.3 Efficient spherical harmonic synthesis at grids residing on the irregular Earth's surface

From the numerical point of view, Eqs. (6), (8) and (12) are computationally intensive to evaluate at densely spaced grids that refer to an irregular surface (e.g., the Earth's topography as in this study). This is caused by the altitude-dependency of the truncation coefficients, implying that different coefficients are needed for points with different elevations. When further combined with the numerical issues associated with the evaluation of $Q_{np}^j(r, \psi_0)$ (cf. Bucha et al, 2019a) as well as with ultra-high-degree spherical harmonic expansions (say, beyond degree 10,800), the direct pointwise evaluation does not appear to be currently possible (even in case of a few hundreds of computation points).

To overcome these difficulties, Bucha et al (2019a) proposed to apply the gradient approach for spherical harmonic synthesis at regular grids residing on irregular surfaces (Holmes, 2003; Balmino et al, 2012; Hirt, 2012). This technique relies on i) an analytical upward/downward continuation from a regular surface to the irregular surface using a Taylor series

and ii) numerically efficient FFT-based algorithms for spherical harmonic synthesis on the regular surface (e.g., sphere or ellipsoid of revolution). In the case of cap-modified spectral modelling, this means that some tens of successive radial derivatives of Eqs. (6), (8) and (12) need to be evaluated for the continuation process (cf. Eqs. 9 and 10 of Bucha et al 2019a). Since the truncation coefficients are the only radius-dependent terms in these relations, we provide in Appendices A and B formulae for an arbitrary radial derivative of all the truncation coefficients from Eqs. (9) – (23). More specifically, we provide spectral relations (Sections A.3 and B.3) and closed relations with a fixed number of terms (A.4 and B.4) for near- and far-zone effects and i) an arbitrary radius r , ii) an arbitrary harmonic degree n , iii) an arbitrary topography power p and iv) an arbitrary order of the radial derivative k . For the sake of brevity, the formulae resulting from the application of the gradient approach to Eqs. (6) – (23) are omitted here, but can readily be obtained analogously to Eqs. (9) and (10) of Bucha et al (2019a).

Finally, Eqs. (6) – (23) can be rewritten such that only a single spherical harmonic synthesis is needed for their evaluation instead of repeating it p_{\max} times, each time with a different maximum degree $p \times n_{\max}$. Taking Eq. (6) as an example, all these relations can be rewritten into a single spherical harmonic synthesis,

$$V^j(r, \varphi, \lambda) = 2\pi G\rho R^2 \sum_{n=0}^N \sum_{m=-n}^n \bar{V}_{nm}^j(r, \psi_0) \bar{Y}_{nm}(\varphi, \lambda), \quad (24)$$

where N is the maximum degree of the synthesis, say, $N = p_{\max} \times n_{\max}$, and the coefficients $\bar{V}_{nm}^j(r, \psi_0)$ can be prepared prior to the synthesis via

$$\bar{V}_{nm}^j(r, \psi_0) = \sum_{p=1}^{p_{\max}} Q_{np}^j(r, \psi_0) \bar{H}_{nmp}, \quad (25)$$

after realizing that (cf. Eq. 53)

$$\bar{H}_{nmp} = 0 \quad \text{for } n > p \times n_{\max}. \quad (26)$$

Furthermore, when combining Eq. (24) with the gradient approach, we found it efficient to compute the $\bar{V}_{nm}^j(r, \psi_0)$ coefficients together with their radial derivatives (necessary for the continuation process) beforehand and store all of them in RAM during the entire synthesis. Although this may require several tens of GBs of RAM, which is certainly true for the synthesis up to degree 21,590 as in our numerical study (cf. Section 4), the gain in computational efficiency may easily outperform costs associated with that amount of RAM. In other words, the time-consuming evaluation of ultra-high-degree fully-normalized Legendre functions needs to be performed only once per synthesis which is a substantial computational acceleration in case of high values of n_{\max} , p_{\max} and N , say, $n_{\max} = 2159$, $p_{\max} = 30$ and $N = 21,590$ as in our numerical study.

4 Numerical experiments

4.1 Truncation coefficients

In this section, we numerically examine the three newly derived groups of truncation coefficients: $Q_{np}^{1,1,j}(r, \psi_0)$, $Q_{np}^{2,1,j}(r, \psi_0)$ and $Q_{np}^{2,2,j}(r, \psi_0)$. The coefficients $Q_{np}^j(r, \psi_0)$ and their higher-order radial derivatives (hence, including $Q_{np}^{1,0,j}(r, \psi_0)$, $Q_{np}^{2,0,j}(r, \psi_0)$, cf. Eqs. 59 and 90, respectively) were discussed in detail in Bucha et al (2019a). In this experiment, we designed parameters of the truncation coefficients such that a high accuracy level could be achieved later in the validation of the cap-modified spectral technique (Section 4.2). By high accuracy, we mean $\sim 0.001 \text{ m}^2 \text{ s}^{-2}$, $\sim \mu\text{Gal}$ and $\sim E$ for the gravitational potential and the components of the gravitational vector and tensor, respectively. The following input parameters are studied here:

- $n = 0, \dots, 21600$ (spherical harmonic degree),
- $p = 1, \dots, 30$ (topography power),
- $k = 0, \dots, 40$ (order of the radial derivative),
- $j = \{\text{'In', 'Out'}\}$ (inside- and outside-cap integration),
- $R = 6,378.137 \text{ km}$ (radius of the reference sphere),
- $r = 6,378.137 \text{ km} + 7 \text{ km}$ (radius of the evaluation sphere to be used as an auxiliary sphere in the gradient approach),
- $\psi_0 = 100 \text{ km}/R \approx 0.90^\circ$ (integration radius).

Note that the evaluation radius r is chosen such that the evaluation sphere passes above all the gravitating masses. This is done in order to avoid possible issues with the slow convergence of the gradient approach in Section 4.2 (see Appendix B of Bucha et al, 2019b). The integration radius ψ_0 , separating the inside- and outside-cap masses, is chosen as 100 km which seems to be a reasonable choice, for instance, for future RTM applications that utilize topography expanded to degree ~ 2159 .

For the numerical evaluation of $Q_{np}^{1,1,j}(r, \psi_0)$, $Q_{np}^{2,1,j}(r, \psi_0)$ and $Q_{np}^{2,2,j}(r, \psi_0)$, we rely in this work on the closed relations from Appendices A.2, A.4, B.2 and B.4 (Eqs. 66, 98 and 99). This because once the coefficients $Q_{np}^j(r, \psi_0)$ from Eq. (6) and their radial derivatives are computed, which is perhaps the most difficult part discussed in Bucha et al (2019a), the truncation coefficients introduced in this paper ($Q_{np}^{1,1,j}(r, \psi_0)$, $Q_{np}^{2,1,j}(r, \psi_0)$ and $Q_{np}^{2,2,j}(r, \psi_0)$) and their radial derivatives can be obtained without any substantial difficulties. Opposed to this, the spectral relations from Appendices A.1, A.3, B.1 and B.3 are here considered as more time-consuming, as they involve i) infinite sums that need to be truncated at ultra-high degrees (e.g., 100,000 in the study of Bucha et al, 2019a) and ii) integrals of products of two ultra-high-degree Legendre functions over a restricted domain.

Following Bucha et al (2019a), we evaluate the $Q_{np}^j(r, \psi_0)$ coefficients and their radial derivatives through recurrence

relations (cf. Bucha et al, 2019a) with 256 significant digits. This rather large number of digits is employed in order to mitigate numerical inaccuracies that are associated with the recurrence relations to evaluate the truncation coefficients (*ibid.*). The computation was conducted in Matlab (www.mathworks.com) using the ADVANPIX toolbox (www.advanpix.com), the latter of which enables to extend the number of significant digits.

Having the $Q_{np}^j(r, \psi_0)$ coefficients and their radial derivatives, we evaluated the coefficients $Q_{np}^{1,1,j}(r, \psi_0)$, $Q_{np}^{2,1,j}(r, \psi_0)$ and $Q_{np}^{2,2,j}(r, \psi_0)$ and their radial derivatives. The entire computation was performed using 256 significant digits and was followed by an indirect accuracy check based on Appendix C. Using 256 significant digits, the validation revealed that the worst agreements for the left-hand and the right-hand sides of Eqs. (107), (108) and (109) were, respectively, 28, 24 and 28 correct digits for the studied values of n , p , k , R , r and ψ_0 (see the first paragraph of this section). To this end, we utilized the measure

$$\delta A = \left| \frac{A - A_{\text{reference}}}{A_{\text{reference}}} \right|, \quad (27)$$

where $A_{\text{reference}}$ represents the right-hand side of Eqs. (107), (108) and (109) and A stands for the left-hand sides of the same equations.

After this, the truncation coefficients were converted into double precision, ensuring an excellent accuracy down to the 15th or 16th digit.

Fig. 1, showing the dependence of $Q_{np}^{1,1,j}(r, \psi_0)$, $Q_{np}^{2,1,j}(r, \psi_0)$ and $Q_{np}^{2,2,j}(r, \psi_0)$ on harmonic degree n and topography power p , indicates some important properties of near-zone coefficients (left panels in Fig. 1).

- The magnitude of the truncation coefficients grows with increasing p (cf. the normalization factors in the subplots of Fig. 1). This could be somewhat anticipated based on the previous experiments with $Q_{np}^j(r, \psi_0)$ and their high-order radial derivatives (Bucha et al, 2019a).
- Contrary to Bucha et al (2019a), where the $Q_{np}^{\text{In}}(r, \psi_0)$ coefficients exhibit a single-wave pattern for $p \geq 2$, the curves for the near-zone coefficients $Q_{np}^{1,1,\text{In}}(r, \psi_0)$, $Q_{np}^{2,1,\text{In}}(r, \psi_0)$ and $Q_{np}^{2,2,\text{In}}(r, \psi_0)$ show multiple short-wavelength waves after, say $p \approx 12$.
- Beyond $p \approx 12$, the near-zone coefficients of lower harmonic degrees are of higher magnitudes and dominate over high-degree coefficients (in a relative sense).
- Within the same type of near-zone coefficients, very similar curves are seen beyond power $p \approx 12$ (up to their signs and the normalization factors, which change substantially).

These observations imply that the near-zone gravity effects will feature strong spatial variations and high maximum de-

grees will be needed in Section 4.2 for their accurate evaluation.

On the other hand, far-zone coefficients (the right panels in Fig. 1)

- show a much reduced variation with respect to harmonic degree (note the different horizontal axes for left and right panels in Fig. 1),
- take the largest values (in a relative sense) in low spectral bands, and
- similarly as the near-zone coefficients, grow in magnitude as the topography power p increases (cf. the normalization factors).

Translated into gravity effects, the first and the second items confirm the known fact that the far-zone gravity effects are mostly of long-wavelength character, and thus can be accurately evaluated with much lower maximum harmonic degrees, provided that ψ_0 is large enough.

In Fig. 2, we show the newly derived truncation coefficients for a fixed topography power $p = 1$ and varying order of the radial derivative k . It reveals that the maximum magnitude of the near-zone coefficients moves towards higher harmonic degrees as the order of the derivative grows. Opposed to this, the far-zone coefficients and their radial derivatives take the largest values in the lower part of the spectrum (say, up to degree 400).

4.1.1 Errors of the indirect check performed in double precision

Despite the high accuracy achieved in the computation of the truncation coefficients in the previous section ($\sim 15 - 16$ digits after conversion into double precision), a catastrophic cancellation may be encountered when evaluating the left-hand side of Eqs. (104), (105), (107), (108), (109) in double precision. Fig. 3 shows that the sum of near- and far-zone coefficients in double precision may not necessarily yield the correct value, even when the coefficients are accurate down to the 16th digit. This is because for some specific combinations of n , p and k , the near- and far-zone coefficients are equal up to many digits (even up to the 16th and beyond) but are of opposite signs. As a result, summing them in double precision may produce, for instance, zero output values, which is apparently an incorrect result when considering the right-hand side of these equations. Taking $Q_{np}^{2,2,j}(r, \psi_0)$ and $p = 20$ from Fig. 3 as an example, this procedure yields zero correct digits up to harmonic degree ~ 2500 , after which the accuracy improves. For $p = 30$, the catastrophic cancellation is observed over the entire studied interval of harmonic degrees (0 - 21,600). These errors then massively deteriorate the accuracy of spherical harmonic synthesis, in which the coefficients are involved. In our numerical study from Section 4.2, prone to these issues are especially the newly derived truncation coefficients $Q_{np}^{1,1,j}(r, \psi_0)$, $Q_{np}^{2,1,j}(r, \psi_0)$ and

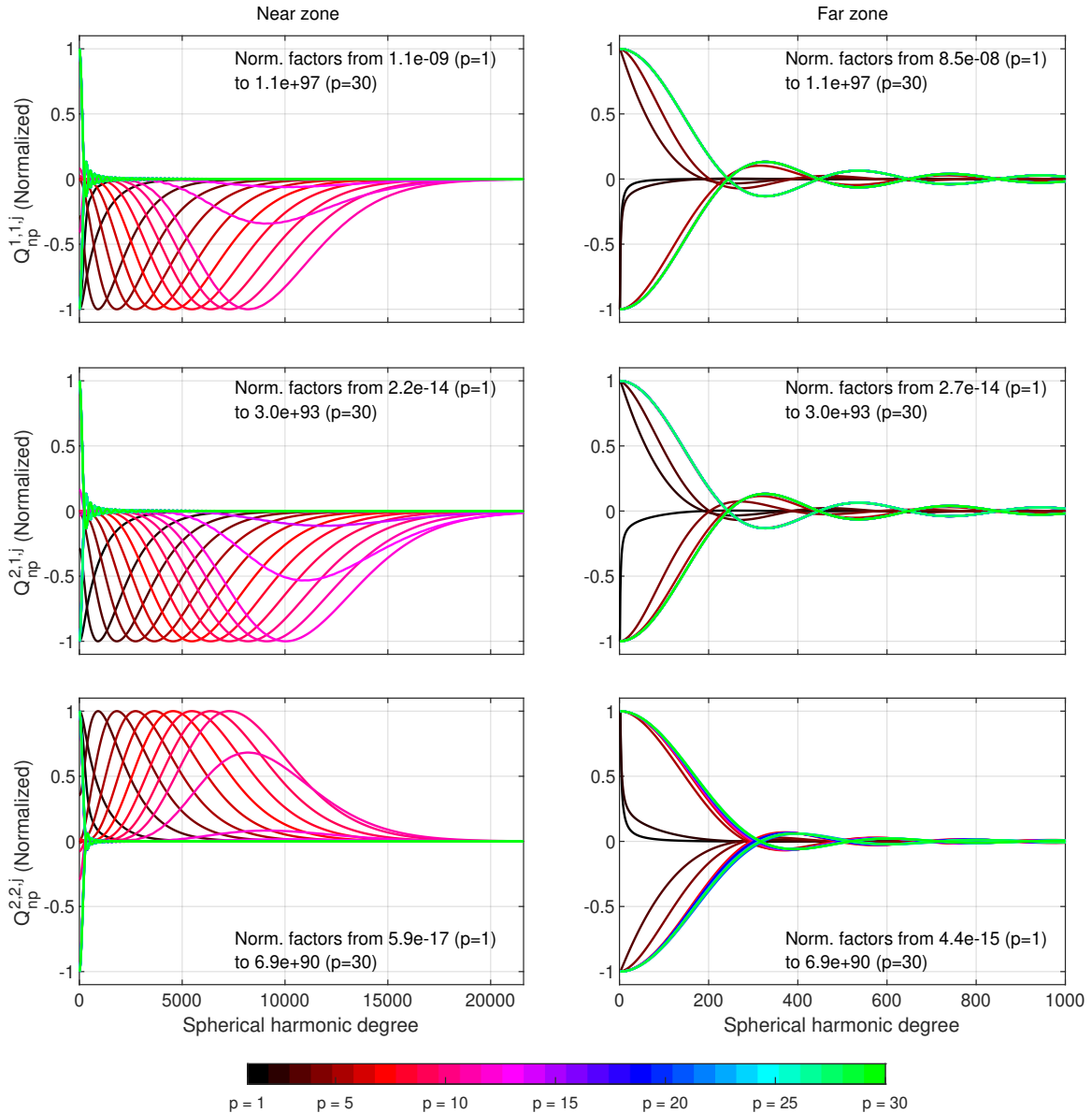


Fig. 1 Normalized truncation coefficients $Q_{np}^{1,1,j}(r, \psi_0)$ (upper row), $Q_{np}^{2,1,j}(r, \psi_0)$ (middle row) and $Q_{np}^{2,2,j}(r, \psi_0)$ (bottom row) evaluated for $R = 6,378,137$ m, $r = 6,378,137$ m + 7000 m, $\psi_0 = 100$ km/R, fixed $k = 0$ and varying p as a function of the harmonic degree. For visualization purposes, the coefficients are normalized by the maximum of their absolute value from the depicted interval. The ranges of the normalization factors are shown in the plots. Note that the curves representing the near-zone coefficients are overlapped at this scale for p beyond, say, 12. Also note that the far-zone coefficients are depicted only up to degree 1000, because they show much reduced variation. The values were prepared in Matlab with 256 digits using the ADVANPIX toolbox

$Q_{np}^{2,2,j}(r, \psi_0)$, implying that a decreased numerical accuracy can be expected for $V_{\cdot}^x, V_{\cdot}y, V_{\cdot}xx, V_{\cdot}xy, V_{\cdot}xz, V_{\cdot}yy, V_{\cdot}yz$ when n, p and k exceed some critical values, which will be determined in the next section.

To overcome this, extended number of significant digits could be employed also in the entire synthesis in cap-modified spectral gravity forward modelling. However, for our multiple ultra-high-degree expansions from Sections 2 and 3, spherical harmonic synthesis at millions of points with, say, 256 digits is far beyond our current computational

capabilities. An alternative approach would be to derive numerically more efficient formulae, but this is left for future work.

In the numerical experiments presented in the next section, we therefore study the effect of the maximum topography power on the final results by using various values of p_{\max} (5, 10, 15, 20 and 30) and N ($n_{\max}, 2 n_{\max}, \dots, 10 n_{\max}$ with $n_{\max} = 2159$) (cf. Eq. 24). In all computations, the truncation coefficients are stored in double precision (16 digits) and the entire cap-modified spectral gravity forward mod-

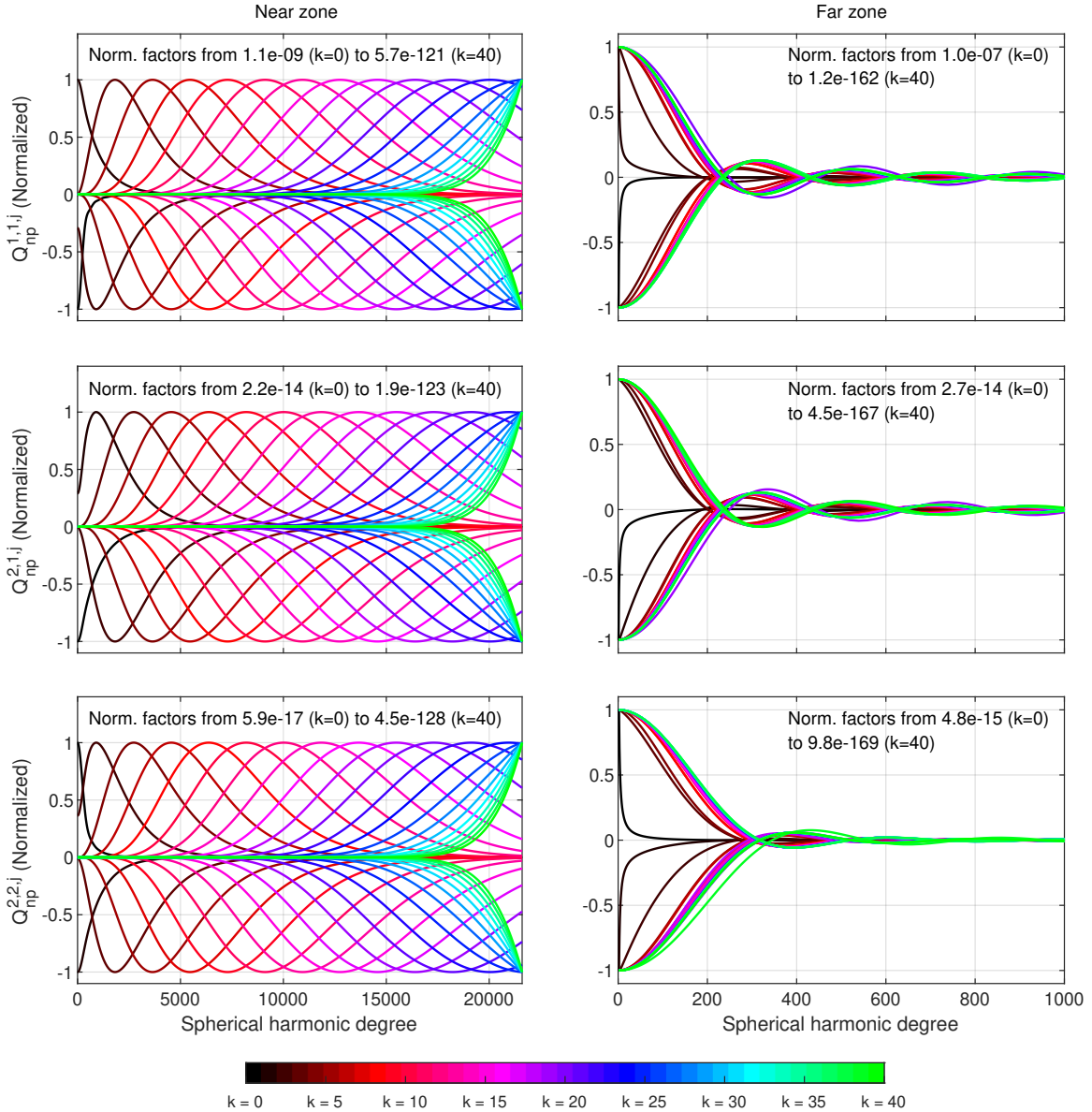


Fig. 2 The same as Fig. 1, but for a fixed $p = 1$ and varying k

elling, that is, the spherical harmonic analysis and the synthesis, are performed in double precision.

4.2 Validation of cap-modified spectral forward modelling using the Earth's degree-2159 topography

To check the correctness of the newly derived equations from Section 3 and Appendices A and B, we designed a numerical test, in which cap-modified spectral modelling is validated against an independent spatial-domain Newtonian integration as a reference. In the experiment, the gravity field is implied by RET2014 (Hirt and Rexer, 2015), which is a model of the Earth's topography based on a surface spherical harmonic expansion up to degree 10,800. The abbreviation

RET stands for the rock-equivalent topography and means that several mass layers with different densities (here, rock, water and ice) were condensed into a single layer equivalent to topographic rock, here with the density $\rho = 2670 \text{ kg m}^{-3}$. For our study, the topography was synthesized up to degree $n_{\max} = 2159$, which approximately corresponds to the 5 arc-min resolution of global gravity field models such as EGM2008 (Pavlis et al, 2012). The implied gravity field is here modelled up to degree $N = 21,590$ (cf. Eq. 24), being the tenth multiple of the topography bandwidth, while employing up to 30 powers of the input topography ($p_{\max} = 30$). This is necessary, because a band-limited topography generates a full-banded gravity field (e.g., Balmino, 1994; Balmino et al, 2012; Hirt and Kuhn, 2014).

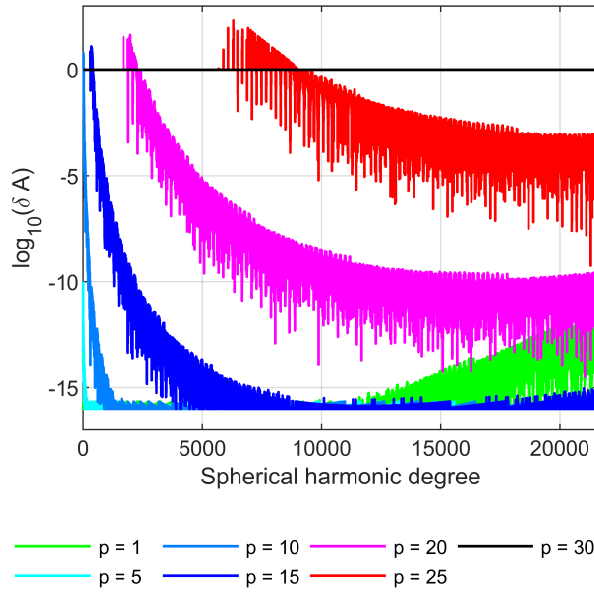


Fig. 3 Indirect check (in double precision) on the numerical accuracy of $Q_{np}^{2,2,j}(r, \psi_0)$ (Eqs. 27 and 109) for $k = 0$ and varying harmonic degree n and topography power p . Contrary to the tests from Section 4.1, here the two terms on the left-hand and the entire right-hand side of Eq. (109) were evaluated with 256 significant digits (accurate up to 28 or more digits) but then each term was separately converted into double precision. After the conversion, the near- and far-zone coefficients were summed in double precision and Eq. (27) was used to compute δA . The base-10 logarithm of δA is shown in the plot. The values of -16 represent the maximum 16-digit accuracy, while 0 and larger values indicate zero accurate digits

Importantly, the settings of the experiment allow us not only to verify the correctness of the equations from Section 3, but also to study the divergence effect of cap-modified spherical harmonic series. While global spectral gravity forward modelling from Section 2 has already been examined for the divergence effect (Hirt et al., 2016; Hirt and Kuhn, 2017; Rexer, 2017), showing its presence for the Earth and Moon when the maximum degree of the spherical harmonic series is large enough, this is the first experiment of its kind for cap-modified spectral modelling.

Spatially, the validation is performed with near-global coverage (within the $[-80^\circ, 80^\circ]$ latitude range) for near-zone gravity effects and, out of necessity, only regionally for the far-zone effects. The latter is done because computational demands associated with delivering reference values via spatial-domain Newtonian integration are enormous when working on a global scale with such high resolutions as in this study. Nevertheless, we evaluated the far-zone effects over two challenging computational areas of the Himalayas (latitude: $[20.05^\circ, 44.96^\circ]$, longitude: $[70.04^\circ, 104.96^\circ]$) and Kiribati ($[-4.95^\circ, 4.96^\circ], [185.04^\circ, 199.96^\circ]$), which can reasonably well serve as a benchmark for the prediction over the entire Earth's surface as long as the values of n_{\max} , p_{\max} and N are similar to ours. These regions were selected, be-

cause they seem to be the most prone to the divergence effect as shown in Hirt et al (2016).

The validation is performed at points arranged in a 5 arc-min equiangular grid which approximately corresponds to the spatial resolution of the degree-2159 topography. The points are distributed globally, excluding 10° polar caps (near-global validation). The radial component of their position is twofold,

- either 1 m above the RET2014 topography H if $H > 0$ m or 1 m above the reference sphere $R = 6,378.137$ km if $H \leq 0$ m, briefly referred to as 1 m above the Earth's surface (Sections 4.2.3 and 4.2.4), and
- on a Brillouin sphere with the radius $R = 6,378.137$ km + 7 km (a sphere being completely outside the masses, Sansò and Sideris, 2013) (Section 4.2.5).

The former set-up enables to identify the divergence effect if present. The latter case, being free of this error by definition, allows us to discriminate a possible divergence effect from errors associated with the evaluation of the truncation coefficients (Section 4.1.1). Note that our spatial-domain Newtonian integration software (Section 4.2.1) is free of the divergence of spherical harmonics and is capable of delivering gravity effects within our target accuracy (cf. Section 4.1) as indirectly shown in Sections 4.2.3, 4.2.5 and 4.2.4. Beyond doubts, the reference values can therefore serve as a benchmark for identifying the divergence effect, similarly as in Hirt et al (2016) or Hirt and Kuhn (2017).

4.2.1 Spatial-domain Newtonian integration

To obtain the reference gravity values, we use spatial-domain Newtonian integration software (cf. Bucha et al, 2016) that combines i) the polyhedron-based routine developed by Tsoulis (2012) and ii) tesseroids (Grombein et al, 2013). The integration radius ψ_0 was set to a spherical distance of 100 km / $6,378.137$ km $\approx 0.90^\circ$.

Near-zone gravity effects. For accurate gravity forward modelling, the integration domain ($0^\circ \leq \psi \leq \psi_0$) is subdivided into an inner zone ($\psi \leq 0.25^\circ$), where we rely on polyhedral modelling, and an outer zone ($0.25^\circ < \psi \leq \psi_0$), being modelled by tesseroids (note that in our case the singularity of the integral kernels of tesseroids does not cause any deterioration that would be larger than our target accuracy specified in Section 4.1, see also Section 4.3.4 of Bucha et al, 2016). Generally, polyhedral gravity forward modelling is slower but more accurate than the tesseroid-based one (e.g., Bucha et al, 2016), so is here used to forward model the crucial innermost masses, and vice versa. The radius of 0.25° that separates the two zones was empirically found to be a reasonable compromise between the accuracy and computational costs. The RET2014 topography was synthesized globally at the spatial resolution of 10 arc-sec, thus with an

oversampling factor of ~ 30 . This grid represents the shape of the topographic masses that were subsequently forward modelled using our Newtonian integration software.

The statistics of the 10 obtained forward modelled quantities ($V^{\text{In}}, V^{\text{x},\text{In}}, V^{\text{y},\text{In}}, V^{\text{z},\text{In}}, V^{\text{xx},\text{In}}, V^{\text{xy},\text{In}}, V^{\text{xz},\text{In}}, V^{\text{yy},\text{In}}, V^{\text{yz},\text{In}}, V^{\text{zz},\text{In}}$) are reported in Table 1. For the sake of brevity, shown in Fig. 4 is only $V^{\text{z},\text{In}}$, which was chosen as representative for visualization purposes, given that it is closely related to the widely used gravity anomalies and disturbances. Note that while the near-zone effects are shown in Fig. 4 over two areas only, the Himalayas and Kiribati, they were computed near-globally within the $[-80^\circ, 80^\circ]$ latitude limit as already discussed. A complete picture of the near-zone reference gravity effects is provided in Figs. S1 – S4 of ESM.

Far-zone gravity effects. In case of far-zone effects, tesseroids are used over the entire integration domain ($\psi_0 \leq \psi \leq 180^\circ$). This is permissible, given the attenuation of gravity signal with increasing distance from the evaluation point. To decrease computation time, the resolution of the forward modelled RET2014 topography is here lowered from 10 arc-sec to 30 arc-sec (oversampling factor of 10) and forward modelling is restricted to two areas, the Himalayas and Kiribati (see Fig. 5 and Table 1). Nevertheless these areas represent a worst-case scenario and are certainly challenging for accurate gravity forward modelling both in the spatial and the spectral domain. The reference far-zone gravity effects are shown for each functional in Figs. S5 – S8 of ESM.

4.2.2 Cap-modified spectral gravity forward modelling

Next, we performed cap-modified spectral gravity forward modelling (Eqs. 6 – 23) on the Earth's topography via the gradient approach (Section 3.3). For the analytical continuation in the gradient approach, we use the radius $6,378,137 \text{ m} + 7000 \text{ m}$ (a sphere outside of all masses) and the Taylor series truncated at $k_{\max} = 40$ (cf. Eq. 9 of Bucha et al, 2019a). The maximum topography integer power is gradually set up to $p_{\max} = 30$. The maximum harmonic degree N (cf. Eq. 24) of the gravity effects varies from n_{\max} to $10n_{\max}$, where $n_{\max} = 2159$. The truncation coefficients were evaluated using 256 significant digits, then they were converted to double precision (cf. Section 4.1) and, finally, the entire harmonic synthesis was conducted in double precision.

Before the validation itself, we show in Fig. 6 dimensionless degree variances (cf. Eq. 15 of Bucha et al, 2019a) of the total near- and far-zone gravity signal $V^{\text{z},j}$ as well as of the individual gravity contributions generated by the p th power of the topography. The quantity $V^{\text{z},j}$ was selected as an example, as it is frequently employed in practice in the form of gravity disturbances. Briefly, both near- and far-zone effects possess an important portion of the signal even well beyond the maximum degree of the topography (cf. Hirt and

Kuhn, 2014; Hirt et al, 2016; Hirt and Kuhn, 2017; Bucha et al, 2019a). Similarly as in Bucha et al (2019a), the degree variances of the far-zone gravity effects exhibit a strong arch-like pattern, which is caused by the Molodensky's truncation coefficients. It is seen that the power of the near-zone gravity signal is stronger and decays more slowly than its far-zone counterpart which is consistent with the decay of gravitational signal with distance from the source (near-zone effects show generally more power in higher frequencies than far-zone effects).

Note that after a certain degree, the curves in Fig. 6 start to oscillate around the same level, e.g., $\sim 10^{-46}$ for near-zone effects and $p \geq 6$ (see also the spectrum of the far-zone effects beyond degree $\sim 15,000$ that is shown by the thick black line). This is caused by numerical issues associated with the growing range of the \bar{H}_{nmp} coefficients (cf. Eq. 4) with increasing p . More specifically, Fig. 7 shows that the algorithms for spherical harmonic synthesis and analysis that we used (the Gauss–Legendre quadrature from Sneeuw 1994 combined with fully-normalized Legendre functions evaluated after Fukushima 2012) were not able to capture such a wide range of magnitudes in double precision. Further examples with similar numerical issues can be seen in Hirt et al (2016) or Bucha et al (2019a). As a potential remedy, the whole computation process could be performed in quadruple precision. This was successfully tested with a degree-360 topography, but it is not used in the final computations with the degree-2159 topography due to its significantly longer computation time. We also tried to normalize the input signal by a single constant factor but without success. Nevertheless, these inferior coefficients can be ignored when the magnitudes they produce are of negligible strengths in terms of gravity (as it is in Fig. 6) or excluded when the numerical inaccuracies are amplified too much as would happen for ultra-high harmonic degrees. Fig. 7 therefore shows that, sooner or later, some different strategy may be required to accurately recover the \bar{H}_{nmp} coefficients for high values of n, m, n_{\max} and p .

4.2.3 Near-zone gravity effects: validation 1 m above the topography

In this validation, the near-zone gravity effects are computed at a 5 arc-min equiangular grid with the radial position of the evaluation points being either 1 m above the RET2014 topography H if $H > 0 \text{ m}$ or 1 m above the reference sphere $R = 6,378.137 \text{ km}$ if $H \leq 0 \text{ m}$. The latter is done to avoid computations inside the masses. In that case, our software for the spatial-domain Newtonian integration would yield (in agreement with potential theory) non-harmonic gravitational potential and its derivatives, while the cap-modified spectral technique, being based on a finite linear combination of harmonic functions (cf. Sections 2 and 3), gives nec-

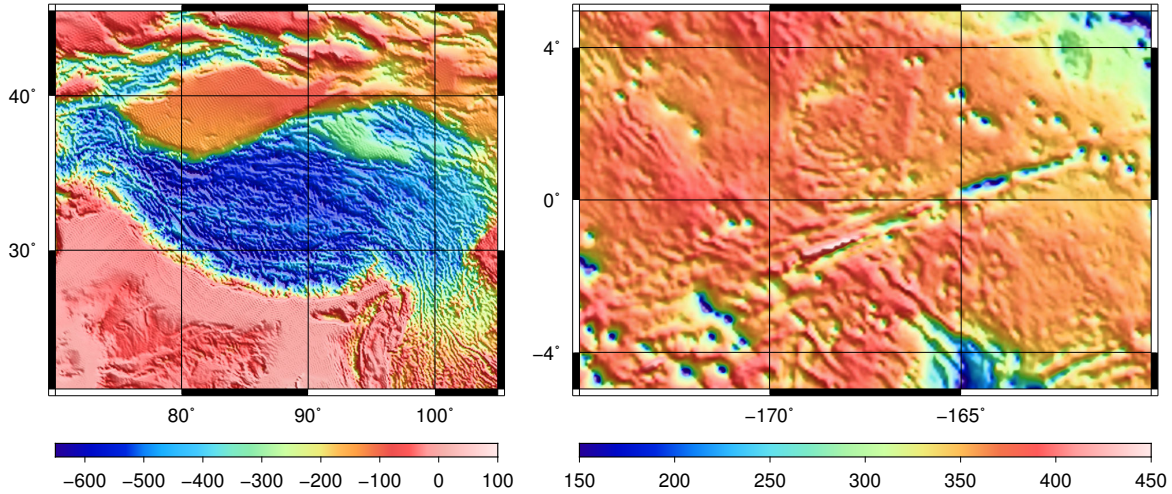


Fig. 4 Near-zone gravitational effects (mGal) implied by the Earth's degree-2159 RET2014 topography in terms of $V^{z,\text{ln}}$ (mGal) over the Himalayas (left panel) and Kiribati (right panel). The computation points are defined by a 5 arc-min equiangular grid and reside 1 m above the Earth's topography (cf. Section 4.2.3). The values were obtained by a divergence-free spatial-domain Newtonian integration and will later serve as a reference for the validation of cap-modified spectral gravity forward modelling. Note that the element $V^{z,\text{ln}}$ represents the positive first-order radial derivative of V^{ln} which is why its sign is opposite with respect to Bucha et al (2019a), who worked with the negative derivative known as the gravity disturbance. The short-scale wavy-like features that can be seen in the left panel, especially around the Himalayas, are caused by the oscillating nature of topography that is expanded in surface spherical harmonics

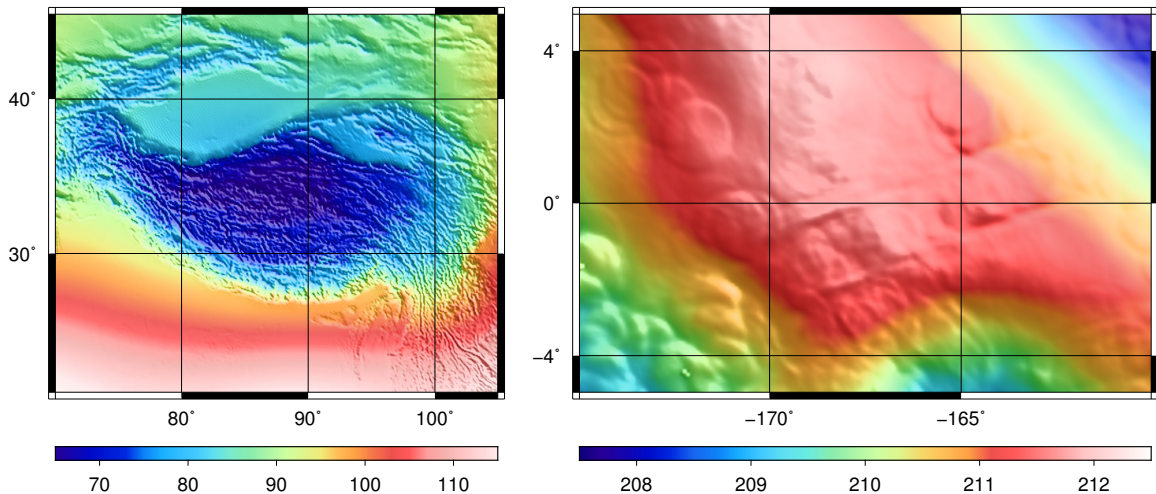


Fig. 5 The same as Fig. 4, but with far-zone gravitational effects (mGal) on $V^{z,\text{ln}}$ over the Himalayas (left panel) and Kiribati (right panel)

essarily a harmonic potential even inside the masses (an analytically downward continued external potential; e.g., Moritz 2010; Freeden and Gerhards 2013), where the true gravitational potential is non-harmonic.

In Table S1 of ESM, we provide statistics of the validation (RMS of the discrepancies and the maximum of their absolute values, here denoted as MAX). For each functional, the obtained discrepancies are plotted in Figs. S9 and S10 of ESM. In Fig. 8, we show the RMS values as a function of the maximum harmonic degree N for various p_{\max} . Several conclusions can be drawn based on the validation.

- V^{ln} (requires $Q_{np}^j(r, \psi_0)$): Within our target accuracy ($\sim 0.001 \text{ m}^2 \text{ s}^{-2}$), the cap-modified harmonic series for the potential converges rather fast when compared with the other quantities. This is not surprising, given that the most significant portion of the gravitational potential signal is contained within its low harmonics, here up to degree ~ 2159 . The best agreement achieved with the least effort is $\text{RMS} = 0.0053 \text{ m}^2 \text{ s}^{-2}$ and $\text{MAX} = 0.035 \text{ m}^2 \text{ s}^{-2}$ and is reached with $p_{\max} = 15$ and $N = 8636$. When translated into geoid undulations, a sub-millimetre RMS accuracy could be achieved in geoid computations. Note that a slightly worse but fairly com-

Table 1 Characteristics of the near- and far-zone reference gravity effects obtained from the spatial-domain Newtonian integration of the degree-2159 RET2014 topography. The computation points are placed 1 m above the Earth's topography (Sections 4.2.3 and 4.2.4). Note that while the statistics for the near-zone effects are based on near-global datasets (5 arc-min equiangular grid within the $[-80^\circ, 80^\circ]$ latitude limits; 1920×4320 nodes), the far-zone statistics are based on two much smaller areas, the Himalayas (300×420 nodes) plus Kiribati (120×180 nodes), representing $\sim 1.8\%$ of grid nodes of the former one. Therefore, the statistics for the far-zone effects likely do not provide a complete global picture of the signals. The abbreviation STD stands for the standard deviation

Quantity	Unit	Near-zone effects				Far-zone effects			
		Min	Max	Mean	STD	Min	Max	Mean	STD
V	$\text{m}^{-2} \text{s}^{-2}$	-490.898	589.679	-139.061	176.223	-26273.726	-9819.973	-13835.625	5259.778
V^x	mGal	-362.166	425.608	-0.356	25.157	-250.559	553.289	100.048	188.022
V^y	mGal	-364.518	368.921	-4.201e-6	24.394	-364.448	272.190	-14.718	109.172
V^z	mGal	-713.520	642.281	140.271	179.917	60.147	211.948	106.818	44.871
V^{xx}	E	-338.470	287.899	7.386	16.628	-18.442	23.440	6.592	11.424
V^{xy}	E	-183.657	160.344	3.569e-3	7.609	-9.174	9.586	-1.492e-2	2.010
V^{xz}	E	-364.062	286.933	7.212e-2	15.679	-2.161	1.020	-0.235	0.445
V^{yy}	E	-403.187	318.051	7.385	16.223	-18.765	29.584	6.680	12.637
V^{yz}	E	-322.009	315.731	2.020e-4	15.391	-0.985	1.170	3.208e-2	0.261
V^{zz}	E	-361.698	659.755	-14.771	28.776	-49.187	36.360	-13.271	23.692

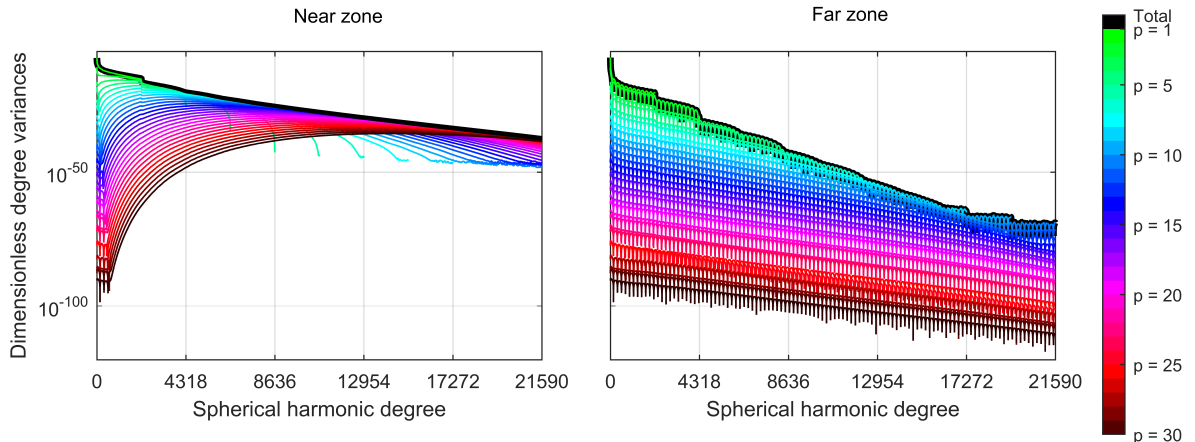


Fig. 6 Dimensionless degree variances (cf. Eq. 15 of Bucha et al, 2019a) of near-zone (up to $\psi_0 \approx 0.90^\circ$) and far-zone (beyond $\psi_0 \approx 0.90^\circ$) gravity effects ($V^{z,j}$) shown as a function of integer power p of the Earth's degree-2159 topography. The degree variances refer to a Brillouin sphere that is outside of all masses with the radius $R = 6,378.137 \text{ km} + 7 \text{ km}$ (the maximum elevation from RET2014 is $\sim 6.7 \text{ km}$ for $n_{\max} = 2159$), where spherical harmonic series converge. No divergence effect can therefore be seen in this figure as opposed to, for instance, Fig. 3.14 of Rexer (2017), who employed global spectral gravity forward modelling ($n_{\max} = 2160$, $p_{\max} = 50$, $N = 21,600$) to provide degree variances referring to the reference sphere that is partially inside the gravitating masses, where spherical harmonic series may converge or diverge

parable sub-millimetre RMS accuracy is seen already with $p_{\max} = 5$ and $N = 4318$ ($\text{RMS} = 0.0054 \text{ m}^2 \text{ s}^{-2}$), but at the cost of a worse MAX value ($0.280 \text{ m}^2 \text{ s}^{-2}$). A careful inspection of Fig. S9 of ESM, where the differences are plotted, reveals that divergence effect emerges over the Himalayas. However, its magnitude is too low to allow us draw reliable conclusions on the divergence of spherical harmonics on the Earth's surface. As can be seen from Figs. S9 and S10, the divergence effect also appears to be present in all other studied quantities, so this observation will not be repeated below. Two exceptions that will be discussed are $V^{x,\text{In}}$ and $V^{z,\text{In}}$, for which the magnitude of the divergence effect is sufficiently large to formulate reliable conclusions.

- $V^{x,\text{In}}, V^{y,\text{In}}$ (both require $Q_{np}^{1,1,j}(r, \psi_0)$): For the two quantities, the lowest RMS errors obtained are 4.1 and 2.7 μGal and were achieved with $p_{\max} = 10$, $N = 10,795$ and $N = 12,954$, respectively. Beyond these values, a massive deterioration is seen, worsening the RMS errors gradually up the order of $\sim 10^{18} \text{ mGal}$ (cf. Table S1 of ESM). However, this is not caused by the divergence effect of spherical harmonics, but instead by the numerical issues related to the evaluation of $Q_{np}^{1,1,j}(r, \psi_0)$ (cf. Section 4.1.1). This conclusion will be confirmed in Section 4.2.5.
- $V^{z,\text{In}}$ (requires $Q_{np}^{1,0,j}(r, \psi_0)$): Using $p_{\max} = 15$ and $N = 15,113$, we achieved a 2 μGal RMS agreement, which is our best result for this quantity. When further increasing the two parameters, especially p_{\max} , the accuracy can slightly be improved over some regions, but the spheri-

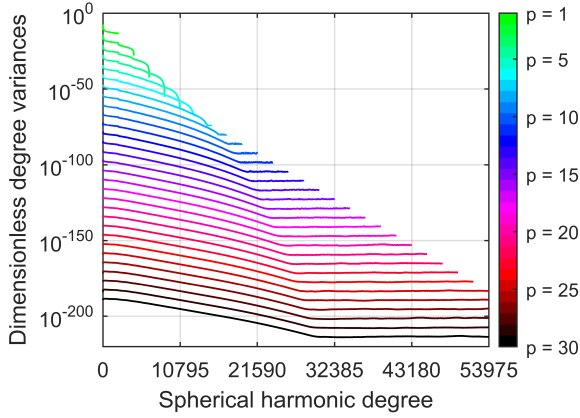


Fig. 7 Dimensionless degree variances of the topographic height function and its first 30 integer powers. The almost horizontal tails of the curves indicate parts of the spectra that were not recovered accurately via spherical harmonic analysis and synthesis in double precision

cal harmonic series starts to produce invalid results over other parts of the Earth's surface. This effect is well visible over the Himalayas (Fig. 9), where increasing p_{\max} results in decreased accuracy with artificial fan-like structures covering large portions of the Earth's surface, similarly as in the studies by Hirt et al (2016), Hirt and Kuhn (2017) and Rexer (2017). The same feature, but of a smaller magnitude, can also be seen over Kiribati when $p_{\max} = 30$. In that case, an area from which the fan-line structure appears to emerge is seen around the latitude -1° and the longitude -168° . The enlarged discrepancies are clearly reflected also in Fig. 8 when $p_{\max} = 30$. At first, the RMS error decreases with N growing up to 10,795 as could be expected, but then the agreement exacerbates from 7.2 μGal up to 11.1 μGal for $N = 19,431$, following by a slight improvement of 10.5 μGal for $N = 21,590$. Even more obvious impact of the divergence effect can be seen in terms of the MAX criterion (cf. Table S1 of ESM), where a sudden degradation starts already with $p_{\max} = 15$ and $N = 15,113$. Supported by these observations as well as by the studies of Hirt et al (2016), Hirt and Kuhn (2017) and Rexer (2017), this behaviour is here concluded to be caused by the divergence effect of spherical harmonics. The numerical issues associated with the evaluation of truncation coefficients from Section 4.1.1 are here rejected as the main cause of these discrepancies. This is justified by experiments that will be presented in Section 4.2.5, where RMS and MAX are shown to drop by 1 and 3 orders of magnitude, respectively, when evaluating $V^{z,\text{In}}$ on a Brillouin sphere, on which the series converges by definition. Nevertheless, even on the Earth's surface expanded up to degree 2159, a 2 μGal near-global RMS value was achieved that

could be considered as satisfactory for current applications.

- $V^{xx,\text{In}}, V^{yy,\text{In}}$ (both require $Q_{np}^{2,0,j}(r, \psi_0)$ and $Q_{np}^{2,2,j}(r, \psi_0)$): For both $V^{xx,\text{In}}$ and $V^{yy,\text{In}}$, we observe RMS errors slightly below 1 E. As already indicated by Fig. 3, increased discrepancies can be expected for large p_{\max} values (cf. Fig. 3). Here, these numerical issues produced RMS errors at the order of $\sim 10^{18}$ E for $p_{\max} = 30$. As will be shown with the $V^{zz,\text{In}}$ element, the errors associated with the $Q_{np}^{2,0,j}(r, \psi_0)$ coefficients are negligible in this case and the bulk of the discrepancies is due to the inaccuracies related to the $Q_{np}^{2,2,j}(r, \psi_0)$ coefficients.
- $V^{xy,\text{In}}$ (requires $Q_{np}^{2,2,j}(r, \psi_0)$): Similarly as in the previous case, sub-E RMS errors were achieved, of which the best one is 0.2 E for $p_{\max} = 10$ and $N = 8636$. Again, the p_{\max} parameter should be chosen carefully, as highly inaccurate results may be obtained (RMS errors at the order of 10^{18} E) when $p_{\max} = 20$ and 30.
- $V^{xz,\text{In}}, V^{yz,\text{In}}$ (both require $Q_{np}^{2,1,j}(r, \psi_0)$): The best RMS agreement with the reference values, 0.079 E and 0.069 E, respectively, was achieved with $p_{\max} = 10$ and $N = 10,795$. Similarly as with the other horizontal derivatives of the gravitational potential that involve differentiation of $Q_{np}^j(r, \psi_0)$ with respect to ψ , spurious artefacts start to be clearly detectable as soon as p_{\max} is high enough (here beyond $p_{\max} = 10$).
- $V^{zz,\text{In}}$ (requires $Q_{np}^{2,0,j}(r, \psi_0)$): For this quantity, we achieved 1.07 E RMS error with $p_{\max} = 10$ and $N = 6477$. As no differentiation of $Q_{np}^j(r, \psi_0)$ with respect to ψ is involved, we do not observe deterioration with increasing p_{\max} and/or N . Similarly as with $V^{z,\text{In}}$, the divergence effect starts to dominate over the signal when $p_{\max} = 30$ and N is larger than, say, 15,113.

4.2.4 Far-zone gravity effects: validation 1 m above the topography

Here, the experiment from the previous section is repeated, but this time we evaluate far-zone gravity effects. The discrepancies are shown in Figs. S13 – S16 of ESM and the statistics are reported in Table S2 (ESM). Briefly, similar accuracy was achieved as with the near-zone effects (RMS of 0.03 m s^{-2} for the potential, 0.8 – 20 μGal for the elements of the gravitational vector and 0.1 – 3 mE for the elements of the gravitational tensor). In all cases except for V , V^x and V^y , the statistics are more favourable, in some cases almost by three orders of magnitude (e.g., V^{zz}). The decreased accuracy in V , V^x and V^y by about one order of magnitude could be explained by the fact that far-zone masses generate in this case signal of larger magnitudes than the near-zone masses (cf. Table 1) which then causes an overall lower accuracy in the absolute sense. However, the relative accuracy remains comparable with the near-zone effects. Also, note

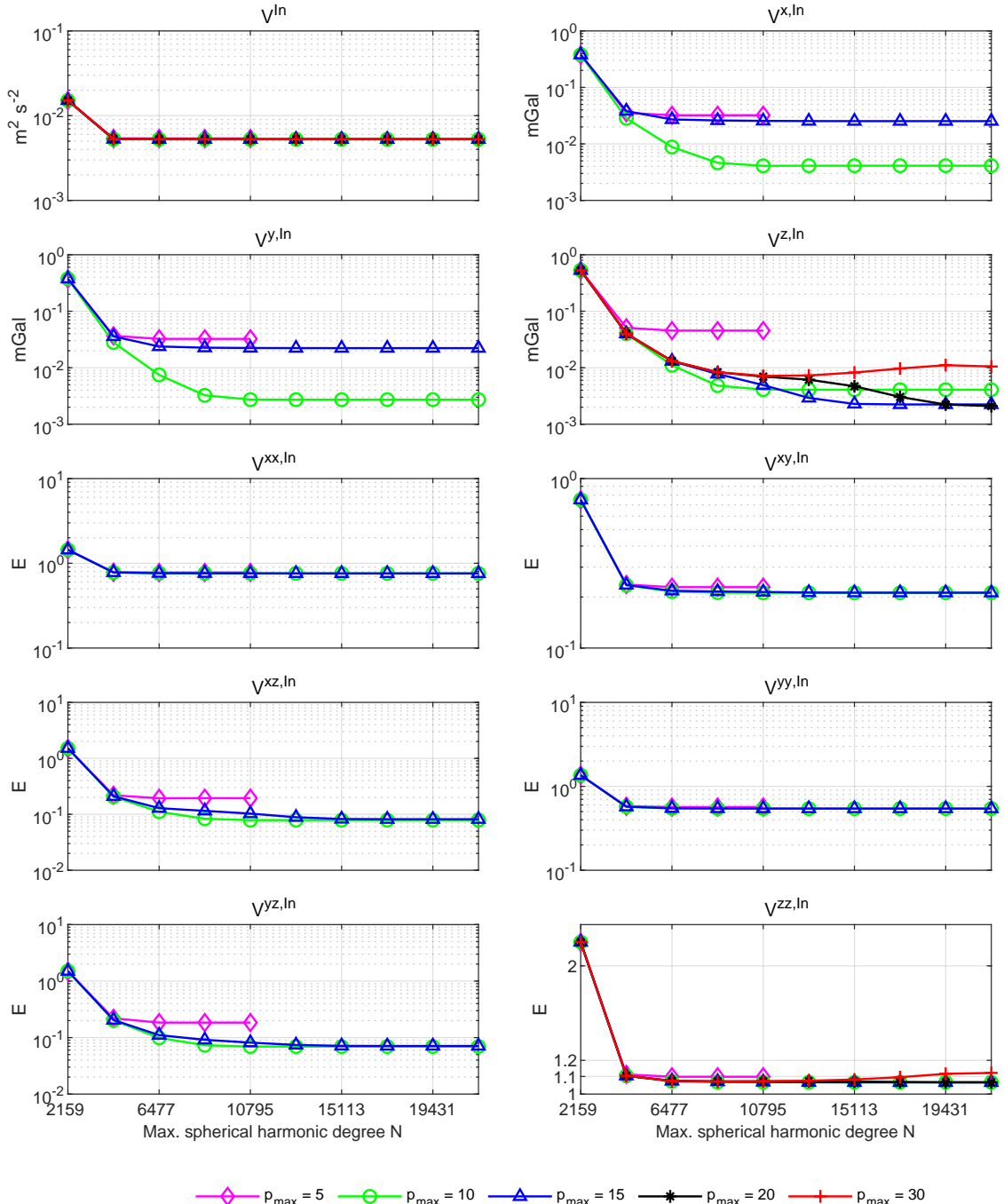


Fig. 8 RMS of discrepancies between the cap-modified spectral technique and the spatial-domain Newtonian integration in terms of near-zone gravity effects evaluated 1 m above the Earth's topography as a function of the maximum degree $N = 2159, 4318, \dots, 21590$ with varying p_{max} (cf. Eqs. 24 and 25). For $V^{x,ln}$, $V^{y,ln}$, $V^{xz,ln}$, $V^{xy,ln}$, $V^{yy,ln}$ and $V^{yz,ln}$, the RMS values significantly exceed the upper limits in the vertical axes when $p_{max} \geq 20$, so are not shown in the plots. These inferior results are caused by the numerical issues associated with the evaluation of the truncation coefficients (cf. Section 4.1.1). Detailed statistics are reported in Table S1 of ESM

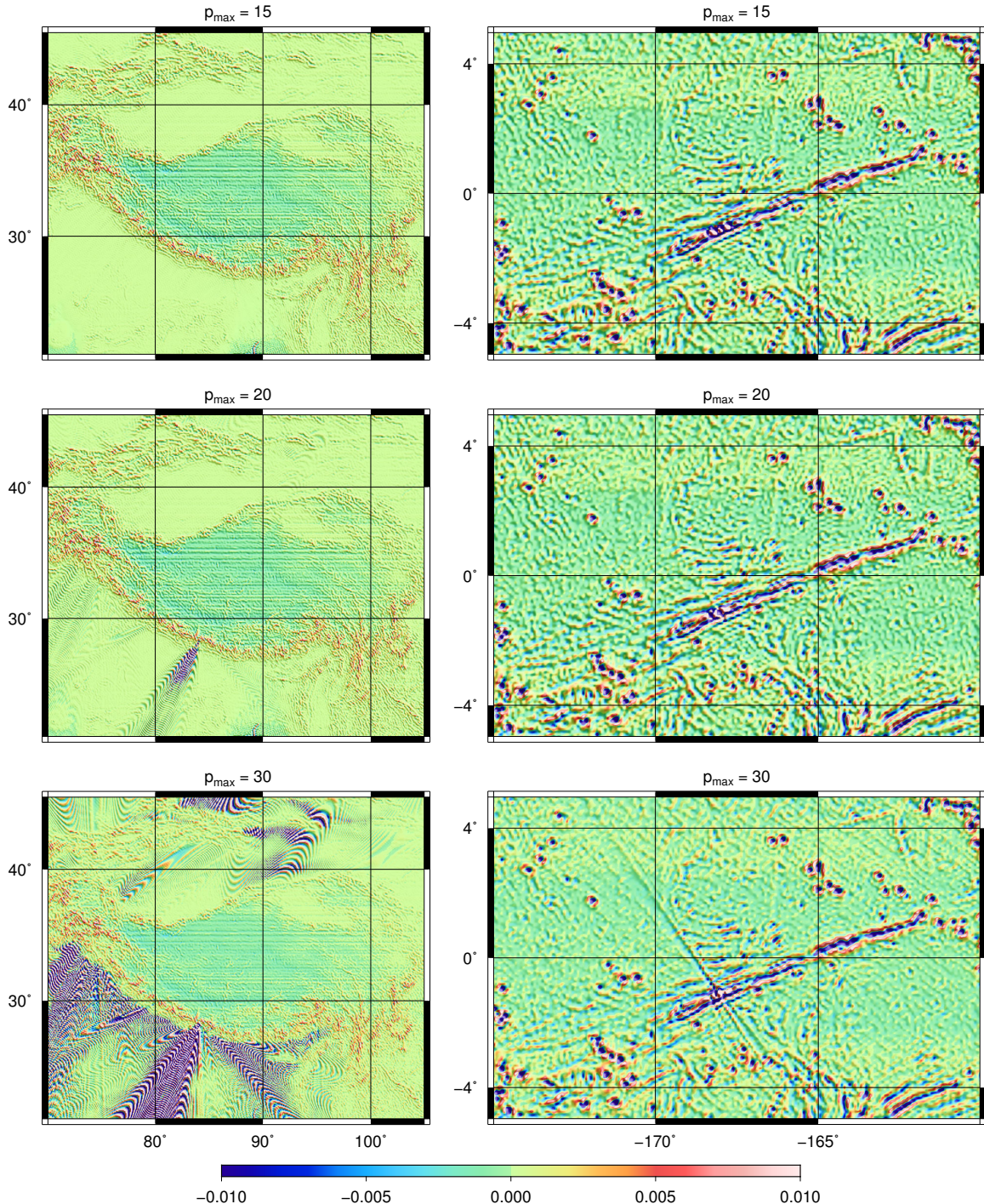


Fig. 9 Near-zone effect differences $V^{z,\text{ln}}$ between cap-modified spectral gravity forward modelling and reference values over the Himalayas (left column) and Kiribati (right column). While the p_{\max} value varies from 15 to 30 in the cap-modified spectral technique, the maximum degree N is fixed to 21,590 (cf. Eq. 24). The computation points are placed 1 m above the topography. Statistics based on the near-global discrepancies can be found in Table S1 of ESM. Unit in mGal

that the far-zone effects are here evaluated only over complex areas of the Himalayas and Kiribati which, as we expect, may worsen the RMS value when compared with the near-global evaluation from the previous section, which included also flat areas of the Earth's surface.

As for the convergence rate, no significant improvement is observed after $p_{\max} = 5$ and $N = 2159$ (cf. Table S2 of ESM), both of which are the lowest values that we study here. Spherical harmonic series therefore converge significantly faster for far-zone effects than for near-zone ones, provided that the integration radius is large enough (here $\psi_0 \approx 0.9^\circ$). This is within the expectations because of the attenuation of short-scale signals with distance. As a result, far-zone effects from the cap-modified spectral technique may require to employ only a first few powers of the topography and the maximum degree may not need to be extended beyond the resolution of the input topography (or at least substantially less than with the near-zone effects). This greatly simplifies the computations and appears to be an analogy to spatial-domain gravity forward modelling, where coarser grid resolutions are used to improve the computational speed when evaluating far-zone effects.

In Fig. 10, we show the discrepancies for $V^{z,\text{Out}}$ as an example. Importantly, despite the high values of p_{\max} and N (30 and 21,590, respectively), no divergence effect is visible as compared to the near-zone effects (the bottom row of Fig. 9), and a sub- μGal accuracy was achieved (cf. Table S2 of ESM). As an explanation, near-zone effects contain more signal power in high harmonics (cf. Fig. 6) which, in turn, may readily cause the divergence effect when evaluating the series on the topography and p_{\max} and N are high enough. Opposed to this, the signal power of far-zone effects is strongest in low and medium harmonics and rather negligible in high-degree harmonics as already discussed.

Similarly as in the Bucha et al (2019a) study, we observe a longitudinal stripe pattern both in Figs. 9 and 10. For now, we still do not have a satisfactory explanation, but we expect that this is most likely caused by numerical inaccuracies associated with the cap-modified spectral technique. These may include the computation of i) the \bar{H}_{nmp} coefficients (cf. Section 4.2.2), ii) the truncation coefficients (Section 4.1.1) or iii) the spherical harmonic synthesis. Nevertheless, the achieved accuracy still seems to be sufficiently high for many current practical applications.

Finally, when $p_{\max} \geq 15$, the results for quantities with at least one horizontal derivative start to deteriorate, indicating that it is difficult to reach a high accuracy in this case. Again, this is caused by the numerical issues related to $Q_{np}^{1,1,j}(r, \psi_0)$, $Q_{np}^{2,1,j}(r, \psi_0)$ and $Q_{np}^{2,2,j}(r, \psi_0)$ (cf. Section 4.1).

4.2.5 Near-zone gravity effects: validation on a Brillouin sphere

Here, we provide the results of the same experiment as in Section 4.2.3 but with the evaluation points placed on a Brillouin sphere having a constant radius of $R_B = 6,378.137 \text{ km} + 7 \text{ km}$ (the maximum elevation from the RET2014 model is $\sim 6.7 \text{ km}$ for $n_{\max} = 2159$). This radius ensures that all evaluation points are located in a space, where the series in Eqs. (6) – (23) converge uniformly and absolutely by definition. Therefore, we assume that if the large discrepancies present in Section 4.2.3 diminish, then they stem from the divergence effect. Otherwise, if the large errors persist, specifically for any of the quantities that involve at least one horizontal derivative, they are assigned to the known numerical issues discussed in Section 4.1.1.

Briefly, it is seen from Fig. 11 that the convergence is now significantly faster than in Fig. 8 and the discrepancies dropped for many of the quantities (cf. Table S3 and Figs. S11 and S12 of ESM). Taking $V^{z,\text{In}}$ with $p_{\max} = 30$ and $N = 21,590$ as an example, the RMS and MAX values decreased from 0.011 mGal and 5.0 mGal to 0.001 mGal and 0.005 mGal, respectively. An improvement is seen also for V^{In} and $V^{zz,\text{In}}$. This supports our conclusion that the increased discrepancies observed in Fig. 9 are indeed caused by the divergence effect.

In case of $V^{x,\text{In}}$, $V^{y,\text{In}}$, $V^{xx,\text{In}}$, $V^{xy,\text{In}}$, $V^{xz,\text{In}}$, $V^{yy,\text{In}}$ and $V^{yz,\text{In}}$, the enlarged discrepancies remain present when $p_{\max} \geq 15$ which shows that these quantities should be computed either with lower values of p_{\max} and N (but still allowing for a high overall accuracy, cf. Section 4.2.3)—or with an extended number of significant digits in the synthesis.

Not shown here, but the evaluation of far-zone effects on a Brillouin sphere is in agreement with the conclusions drawn in this section.

4.2.6 Concluding remarks on the validation

First, it is obvious that our experiments with truncated spherical harmonic series (Eqs. 6 – 23) cannot in principle reveal whether the original infinite series converge or diverge. This is because what we actually deal with in practice is in fact a finite series of real numbers, which necessarily converges to a real number. When we speak about the divergence effect, we refer to a series behaviour yielding for a certain maximum degree N_1 a worse approximation of the true value than for some $N_2 < N_1$. Note that this, however, differs from the definition of divergent infinite series. As a consequence, even a series suffering from the divergence effect may indeed converge to the true value when extended up to infinity (for instance, this appears to be the case of the Taylor series in Figs. 5 and 9 of Balmino et al 2012 and Bucha et al 2019b, respectively). Nevertheless, for some applications in

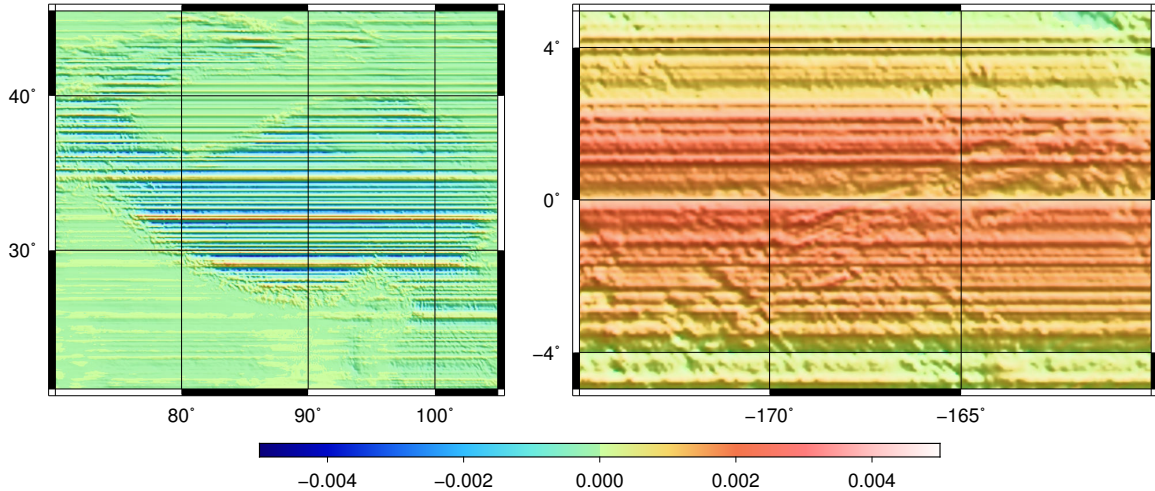


Fig. 10 Far-zone effect differences $V^z,_{\text{Out}}$ between cap-modified spectral gravity forward modelling and reference values over the Himalayas (left column) and Kiribati (right column). In both cases, the $p_{\max} = 30$ and $N = 21,590$ were used in the synthesis (cf. Eq. 24). The computation points are placed 1 m above the topography. Statistics of the discrepancies can be found in Table S2 of ESM. Unit in mGal

physical geodesy, the divergence effect is not a desired behaviour and should be identified if present. In case of, for instance, RTM study, it could lead to grossly invalid results with respect to the observed terrestrial gravity. If the series in Eqs. (6) – (23) are divergent when extended up to infinity but are able to represent the true value with a [...] *high degree of accuracy* [...] (Gradshteyn and Ryzhik, 2007) after a suitable truncation, then they can be considered as asymptotic (e.g., Sjöberg, 1977; Moritz, 2003; Gradshteyn and Ryzhik, 2007; Sjöberg and Bagherbandi, 2017).

Second, our validation is performed at a 5 arc-min equiangular grid, while the gravity signals, here expanded up to degree 21,590, possess spatial information down to the ~ 30 arc-sec resolution. Our experiments are thus not able to examine whether the divergence effect is present, roughly speaking, inside the cells of the 5 arc-min grid.

Third, our experiments are not capable of revealing the divergence effect at magnitudes close to, say, the μGal -level for gravity if present. This is because the $\sim \mu\text{Gal}$ accuracy of the two techniques is not sufficient to draw such conclusions reliably.

Finally, our experiments were restricted to studying the divergence effect for gravity field expanded up to degree 21,590. As a consequence, they cannot be used to extrapolate the series behaviour beyond that degree. These conclusions are therefore valid only for the degree-2159 RET2014 topography with the near- and far-zone gravity effects ($\psi_0 \approx 0.90^\circ$) modelled up to degree 21,590. However, it seems to be reasonable to extend this conclusion from one particular degree-2159 model, here RET2014, to all topographic models expanded up to the same maximum degree. This is because they all share similar spectral properties, and therefore similar behaviour of the divergence effect can be expected.

Importantly, this generalization is proposed exclusively for the Earth's topographic models and not generally also for other bodies like, for instance, the Earth's Moon. This reflects the fact that a different planetary surface may produce a substantially different behaviour of the divergence effect (cf. Hirt et al., 2016; Hirt and Kuhn, 2017; Rexer, 2017).

As a general conclusion, based on the tests from Sections 4.2.3, 4.2.4 and 4.2.5, we are confident in saying that the enlarged discrepancies in V^z and V^{zz} from Section 4.2.3 are caused by the divergence effect of spherical harmonics, while in case of V^x , V^y , V^{xx} , V^{xy} , V^{xz} , V^{yy} , V^{yz} and $p_{\max} \geq 20$, they originate from numerical issues associated with ultra-high degree cap-modified spectral modelling. Nevertheless, using appropriate values for p_{\max} and N , accuracy that appears to be sufficient for many practical applications was achieved in this study over the entire Earth's surface in both cases ($\sim 0.1 \text{m}^2 \text{s}^{-2}$ for the gravitational potential, $\sim \mu\text{Gal}$ for the gravitational vector and $\sim \text{E}$ for the gravitational tensor elements).

5 Conclusions

This paper extends cap-modified spectral gravity forward modelling from the ability of delivering gravitational potential and its radial derivatives (presented by Bucha et al., 2019a) to the full gravitational vector and tensor in the local north-oriented reference frame. In addition, equations for all radial derivatives of the horizontal components are provided.

Using advanced forward modelling methods, algorithms and computational resources, the new technique has been successfully validated in a numerical experiment for all 10 gravity field quantities against an independent and divergence-free spatial-domain forward modelling. The gravitating body,

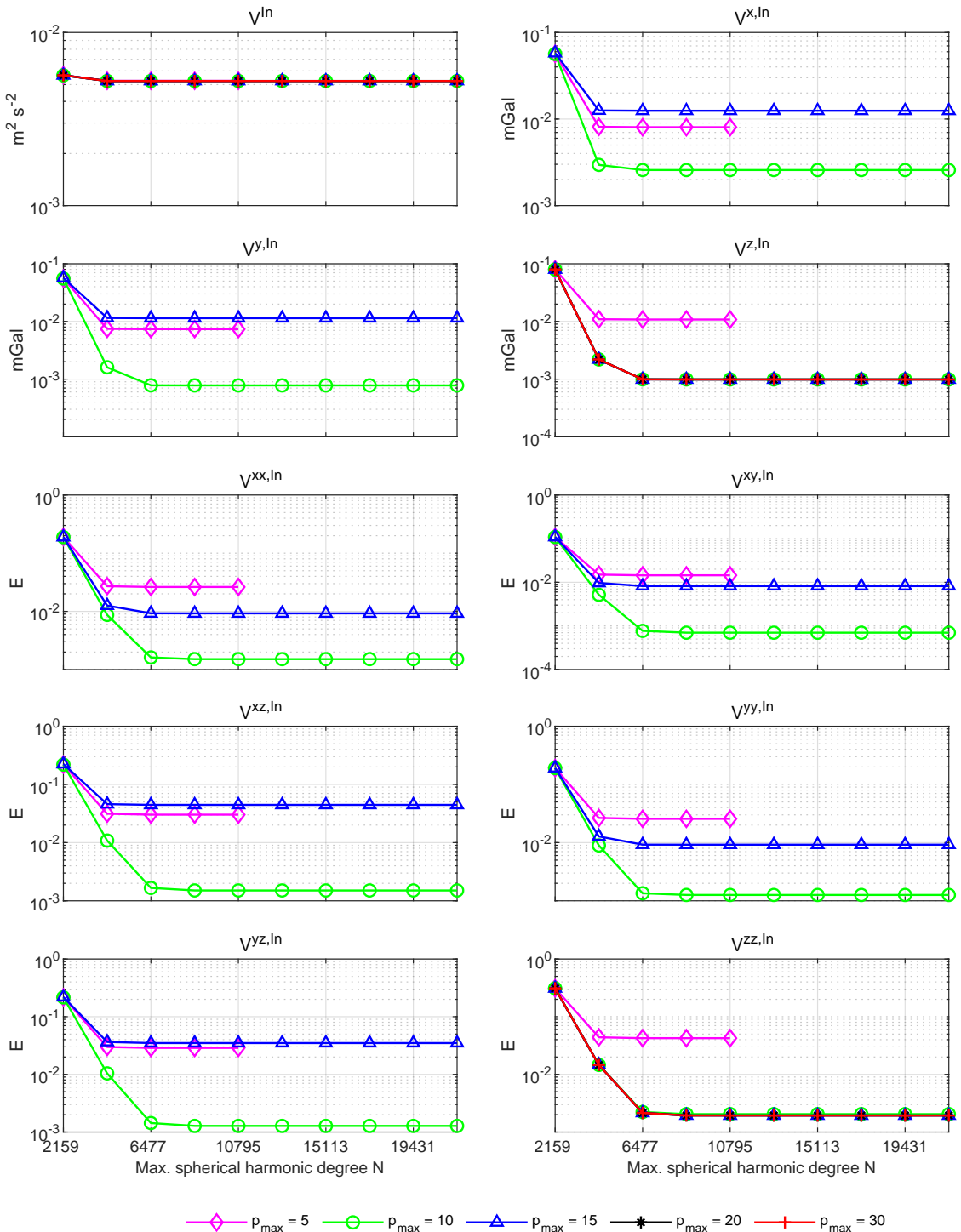


Fig. 11 RMS of discrepancies between the cap-modified spectral technique and the spatial-domain Newtonian integration in terms of near-zone gravity effects evaluated on a Brillouin sphere (radius $R_B = 6,378.137 \text{ km} + 7 \text{ km}$) as a function of the maximum degree $N = 2159, 4318, \dots, 21590$ with varying p_{\max} (cf. Eqs. 24 and 25). For $V^{x,ln}$, $V^{y,ln}$, $V^{xx,ln}$, $V^{xy,ln}$, $V^{xz,ln}$, $V^{yy,ln}$ and $V^{yz,ln}$, the RMS values significantly exceed the upper limits in the vertical axes when $p_{\max} \geq 20$, so are not shown in the plots. These inferior results are caused by the numerical issues associated with the evaluation of the truncation coefficients (cf. Section 4.1.1). Detailed statistics are reported in Table S3 of ESM

the Earth's degree-2159 topography, was forward modelled, yielding its implied gravity field up to degree 21,590. One of the most challenging steps was the accurate calculation of truncation coefficients up to ultra-high degrees (here 21,600), high integer powers of the topography (30) and high-order radial derivatives of the truncation coefficients (40). To this end, we had to extend the number of significant digits from 16 in double precision to 256 digits. This rather huge number of digits ensured numerical evaluation of the coefficients with 24-digit or better accuracy. Despite this fairly sufficient number of common digits in terms of double precision, we have found out that the loss of significance may occur for rather advanced but realistic conditions. To avoid these issues, one can lower the maximum topography power p_{\max} and maximum harmonic degree N for the most problematic coefficients $Q_{np}^{1,1,j}$, $Q_{np}^{2,1,j}$, $Q_{np}^{2,2,j}$ and still obtain acceptable accuracy. Using this strategy, we obtained RMS errors at the level of $0.005 \text{ m}^2 \text{ s}^{-2}$ (gravitational potential), $4 \mu\text{Gal}$ (gravitational vector) and $0.07 - 1 \text{ E}$ (gravitational tensor) for near-zone effects, and similar accuracy was achieved for the far-zone effects ($0.03 \text{ m}^2 \text{ s}^{-2}$, $0.8 - 20 \mu\text{Gal}$, $0.1 - 3 \text{ mE}$, respectively). In the former case, we used i) $p_{\max} = 10$ (in some cases 15) topography powers, ii) the maximum degree of $N = \sim 10,795$ and iii) $k_{\max} = 40$ radial derivatives for the continuation in the gradient approach. In the latter case, a higher convergence rate was observed and thus significantly lower values of p_{\max} and N were sufficient while keeping a comparable accuracy (10 and 2159, respectively; k_{\max} might also be lowered, but this was not studied). Together with other indirect validations discussed in the manuscript, these results demonstrate the correctness of the newly derived equations. It needs to be stressed, however, that avoiding the numerical issues by lowering p_{\max} and N may not be an acceptable strategy for more complex topographies than that in our study ($n_{\max} > 2159$).

The demanding character of our numerical experiments was drawn by the intention to study the convergence/divergence behaviour of both global and cap-modified spectral gravity forward modelling on the topography. We have shown that a severe divergence effect can be observed when the spherical harmonic series are evaluated on the Earth's surface, a region in which the series may no longer converge. We have also demonstrated that the issue becomes more serious when improving the completeness of the modelled gravity field, that is, when increasing the p_{\max} and N parameters. Including findings from other recent studies (e.g., Garmier and Barriot, 2001; Takahashi and Scheeres, 2014; Hu and Jekeli, 2015; Hirt et al., 2016; Reimond and Baur, 2016; Sebera et al., 2016; Hirt and Kuhn, 2017; Rexer, 2017; Bucha et al., 2019b; Chen et al., 2019), the divergence issue of spherical harmonic series on planetary surfaces may soon become a more urgent issue than perhaps expected before. To be more specific, this study has shown that the divergence ef-

fect comes into play at least around degree 10,795 in terms of RMS errors (see also the degree variances in Fig. 3.14 of Rexer 2017). We expect that the divergence effect may be detectable at even lower degrees if $p_{\max} > 30$. Therefore, as we believe, various spherical harmonic representations of the true potential in the vicinity of the field-generating body (e.g., Sacerdote and Sansò, 2010; Sansò and Sideris, 2013; Bucha et al., 2019b) should further be examined to enable reliable spherical harmonic gravity field modelling close to the Earth's surface. In the space external to the smallest sphere enclosing all gravitating masses, spherical harmonic series are, however, convergent as known from potential theory (e.g., Hotine, 1969).

As an outlook on further developments in cap-modified spectral modelling, the probably most urgent issue is the accurate and efficient evaluation of Molodensky's truncation coefficients for high values of n , p and k . As shown in this paper, more than 200 significant digits can easily be lost when targeting at high values for n , p and k . In terms of the computational speed, it took about one week to compute the near- and far-zone coefficients using a PC with Intel®Core™i7-6800K CPU, 128 GB of RAM and a 250 GB SSD drive (our code is not parallelized because its most time-consuming parts involve recurrence relations). Because of this, we decided to release the final sets of truncation coefficients that were used in this study (cf. Data availability after this section), making it possible for others to reuse them and thus avoid the somewhat cumbersome computations with 256 significant digits. The next issue, which will become relevant for a further development of spectral gravity forward modelling techniques, was illustrated in Fig. 7. The figure implies that high powers of the topographic height function may be difficult to accurately evaluate, because they cover a wide range of magnitudes which may be problematic when standard algorithms for harmonic analysis and synthesis are used in double precision. This was not recognized in previous works on global and cap-modified spectral forward modelling. Next, the observed loss of significance indicate that our strategy may need to be modified if one intends to extend the modelling beyond the levels of resolution and completeness of the modelling reached in this paper. Besides these computational and numerical challenges, a study on the relation between the divergence effect and the integration radius could be beneficial. It might reveal, for instance, an integration radius (possibly multiple radii depending on the location) for which the series for far-zone effects start to suffer from the divergence effect on a detectable level in a closed-loop environment.

Author contributions: BB, CH and MK designed the study; BB conducted all the numerical experiments and drafted the manuscript; all authors discussed and commented on the manuscript.

Data availability: *Input data:* The input RET2014 topography (Hirt and Rexer, 2015) is available at <http://ddfe.curtin.edu.au/models/> Earth2014.

Output data: Gravity effects from spatial and spectral gravity forward modelling and spherical harmonic coefficients of 30 integer powers of the degree-2159 RET2014 topography are available on the request from BB (~ 400 GB). The evaluated truncation coefficients $Q_{np}^j, Q_{np}^{1,0,j}, Q_{np}^{1,1,j}, Q_{np}^{2,0,j}, Q_{np}^{2,1,j}, Q_{np}^{2,2,j}$ are available for download at <http://edisk.cvt.stuba.sk/~xbuchab/>.

Computer codes: Each of the following routines is written in Matlab and was tested with Matlab R2015b and R2018b. The software packages for spherical harmonic synthesis, GrafLab (Bucha and Janák, 2013) and isGrafLab (Bucha and Janák, 2014), routines to perform ultra-high-degree surface spherical harmonic analysis and to compute truncation coefficients $Q_{np}^j, Q_{np}^{1,0,j}, Q_{np}^{1,1,j}, Q_{np}^{2,0,j}, Q_{np}^{2,1,j}, Q_{np}^{2,2,j}$ are available at <http://edisk.cvt.stuba.sk/~xbuchab/>.

Acknowledgements BB was supported by the project VEGA 1/0750/18. The computations were performed at the HPC centre at the Slovak University of Technology in Bratislava and at the Slovak Academy of Sciences, which are parts of the Slovak Infrastructure of High Performance Computing (SIVVP project, ITMS code 26230120002, funded by the European region development funds, ERDF). The maps were produced using the Generic Mapping Tools (Wessel and Smith, 1998).

A Derivation of the first-order potential derivatives in LNOF for cap-modified spectral gravity forward modelling

In this appendix, cap-modified spectral gravity forward modelling is presented for the first-order potential derivatives in LNOF, including the horizontal ones. For the sake of brevity, the derivation is shown only for the near-zone gravitational effects (inside-cap integration). For the far-zone effects (outside cap integration), we provide only the final formulae, because the derivation can easily be reproduced, simply by changing the integration domain. Our derivation is based on the idea by Molodensky et al (1962) and follows the manner by, for instance, Heiskanen and Moritz (1967) and Šprlák et al (2015).

The starting point is the expression for the topographic potential induced by topographic masses that have a constant mass density ρ and are located inside a spherical cap centred at the evaluation point (Bucha et al, 2019a),

$$V^{\text{In}}(r, \varphi, \lambda) = G\rho R^2 \sum_{p=1}^{\infty} \int_{\psi=0}^{\psi_0} \int_{\alpha=0}^{2\pi} H^p(\psi, \alpha) K_p(r, \psi) \times \sin \psi d\alpha d\psi, \quad (28)$$

where ψ and α are the spherical distance and azimuth, respectively, $\psi_0 \in [0, \pi]$ is the spherical distance defining the spherical cap and $H^p(\psi, \alpha)$ is the p th integer power of the topographic height function (cf. Eq. 4). For $r > R$, the integral kernels $K_p(r, \psi)$ can be express either via a spectral

relation

$$K_p(r, \psi) = \sum_{n=0}^{\infty} \left(\frac{R}{r} \right)^{n+1} \frac{\prod_{r=1}^p (n+4-r)}{p!(n+3)} P_{n,0}(\cos \psi), \quad (29)$$

where $P_{n,0}$ is the un-normalized Legendre function of degree n , or through closed spatial formulae

$$\begin{aligned} K_1(r, \psi) &= \frac{R}{l(r, \psi)}, \\ K_2(r, \psi) &= \frac{1}{2} \left(K_1(r, \psi) - r \frac{\partial K_1(r, \psi)}{\partial r} \right), \\ K_p(r, \psi) &= \frac{1}{p!} \sum_{s=1}^{p-2} a_{ps} r^{p-s} \frac{\partial^{p-s} K_1(r, \psi)}{\partial r^{p-s}}, \quad p \geq 3, \end{aligned} \quad (30)$$

with the Euclidean distance

$$l(r, \psi) = \sqrt{r^2 - 2Rr \cos \psi + R^2} \quad (31)$$

and the coefficients

$$a_{ps} = (-1)^{p-1} \frac{(p-1)!(p-3)!}{(p-s)!(p-s-2)!(s-1)!}. \quad (32)$$

Spatial and spectral relations for the radial derivatives of $K_p(r, \psi)$, $p \geq 1$, are provided in Appendix A.4 (Eqs. 67 and 70, respectively).

Throughout all the derivations in Appendices A and B, we assume that

$$r > \max(R + \hat{H}(\varphi, \lambda)), \quad (33)$$

ensuring that the order of summation and integration can be interchanged whenever necessary. Then, the resulting infinite spherical harmonic series for the topographic potential and its derivatives are absolutely and uniformly convergent. Otherwise, the series may converge or diverge.

Next, we formally extend the cap integration from Eq. (28) to the whole sphere. This can be achieved with discontinuous integral kernels

$$K_p^{\text{In}}(r, \psi) = \begin{cases} K_p(r, \psi) & \text{for } 0 \leq \psi \leq \psi_0, \\ 0 & \text{for } \psi_0 < \psi \leq \pi, \end{cases} \quad (34)$$

and leads to

$$\begin{aligned} V^{\text{In}}(r, \varphi, \lambda) &= G\rho R^2 \sum_{p=1}^{\infty} \int_{\psi=0}^{\pi} \int_{\alpha=0}^{2\pi} H^p(\psi, \alpha) K_p^{\text{In}}(r, \psi) \\ &\quad \times \sin \psi d\alpha d\psi. \end{aligned} \quad (35)$$

Note that the gravitational potential in Eq. (35) still remains to be implied only by the inside-cap masses despite the global integration (cf. the zero case for $K_p^{\text{In}}(r, \psi)$ in Eq. 34).

To obtain the sought first-order derivatives of $V^{\text{In}}(r, \varphi, \lambda)$ in LNOF, we introduce the following differential operators (e.g., Heiskanen and Moritz, 1967),

$$\begin{aligned}\mathcal{D}^x &= \frac{1}{r} \frac{\partial}{\partial \varphi} = -\cos \alpha \mathcal{D}^{1,1}, \\ \mathcal{D}^y &= -\frac{1}{r \cos \varphi} \frac{\partial}{\partial \lambda} = \sin \alpha \mathcal{D}^{1,1}, \\ \mathcal{D}^z &= \mathcal{D}^{1,0},\end{aligned}\quad (36)$$

where we utilized the relations (ibid.)

$$\begin{aligned}\frac{\partial}{\partial \varphi} &= -\cos \alpha \frac{\partial}{\partial \psi}, \\ \frac{1}{\cos \varphi} \frac{\partial}{\partial \lambda} &= -\sin \alpha \frac{\partial}{\partial \psi},\end{aligned}\quad (37)$$

and introduced the substitutions

$$\begin{aligned}\mathcal{D}^{1,0} &= \frac{\partial}{\partial r}, \\ \mathcal{D}^{1,1} &= \frac{1}{r} \frac{\partial}{\partial \psi} = -\frac{1}{r} \sin \psi \frac{\partial}{\partial \cos \psi}.\end{aligned}\quad (38)$$

In Eq. (38), the first superscript next to \mathcal{D} , here being equal to 1, implies that the differential operator is related to the first-order derivatives of the gravitational potential. The second superscript denotes the order of the differentiation with respect to ψ (here either 0 or 1). Importantly, the two expressions for $\mathcal{D}^{1,1}$ are equal when considering that $\mathcal{D}^{1,1}$ will only be applied to isotropic kernels $K_p(r, \psi)$ (cf. Eqs. 29 and 30), each of which can generally be expressed by a convergent series

$$\mathcal{K}(r, \psi) = \sum_{n=0}^{\infty} \left(\frac{R}{r}\right)^{n+1} k_n P_{n,0}(\cos \psi), \quad r > R. \quad (39)$$

After applying the differential operators from Eq. (36) to the gravitational potential from Eq. (35), the first-order derivatives of V^{In} in LNOF are obtained as

$$\begin{aligned}V^{v,\text{In}}(r, \varphi, \lambda) &= G \rho R^2 \sum_{p=1}^{\infty} \int_{\psi=0}^{\pi} \int_{\alpha=0}^{2\pi} H^p(\psi, \alpha) K_p^{v,\text{In}}(r, \psi) \\ &\quad \times \sin \psi d\alpha d\psi, \quad v = \{x, y, z\},\end{aligned}\quad (40)$$

where the integral kernels

$$K_p^{v,\text{In}}(r, \psi) = \mathcal{D}^v K_p^{\text{In}}(r, \psi), \quad v = \{x, y, z\}, \quad (41)$$

read

$$\begin{aligned}K_p^{x,\text{In}}(r, \psi) &= -\cos \alpha K_p^{1,1,\text{In}}(r, \psi), \\ K_p^{y,\text{In}}(r, \psi) &= \sin \alpha K_p^{1,1,\text{In}}(r, \psi), \\ K_p^{z,\text{In}}(r, \psi) &= K_p^{1,0,\text{In}}(r, \psi),\end{aligned}\quad (42)$$

with

$$K_p^{1,i,\text{In}}(r, \psi) = \mathcal{D}^{1,i} K_p^{\text{In}}(r, \psi), \quad i = 0, 1. \quad (43)$$

Eq. (42) reveals that the three integral kernels $K_p^{v,\text{In}}(r, \psi)$, $v = \{x, y, z\}$, from Eq. (40) can be expressed in terms of two kernels only, $K_p^{1,i,\text{In}}(r, \psi)$, $i = 0, 1$. As a result, only two sets of Molodensky's truncation coefficients are now needed to compute the three elements of the gravitational vector (see also Šprlák et al, 2015).

Next, the kernels $K_p^{1,i,\text{In}}(r, \psi)$ are expanded in series of un-normalized Legendre functions of the first kind (e.g., de Witte, 1967; Šprlák et al, 2015),

$$K_p^{1,i,\text{In}}(r, \psi) = \sum_{n=i}^{\infty} \frac{2n+1}{2} Q_{np}^{1,i,\text{In}}(r, \psi_0) P_{n,i}(\cos \psi), \quad i = 0, 1. \quad (44)$$

The coefficients $Q_{np}^{1,i,\text{In}}(r, \psi_0)$ are called Molodensky's truncation coefficients and are defined as (ibid.)

$$\begin{aligned}Q_{np}^{1,i,\text{In}}(r, \psi_0) &= \frac{(n-i)!}{(n+i)!} \int_0^{\pi} K_p^{1,i,\text{In}}(r, \psi) P_{n,i}(\cos \psi) \sin \psi d\psi \\ &= \frac{(n-i)!}{(n+i)!} \int_0^{\psi_0} \mathcal{D}^{1,i} K_p(r, \psi) P_{n,i}(\cos \psi) \sin \psi d\psi,\end{aligned}\quad (45)$$

where $i = 0, 1$. Formulae suitable for practical evaluation of these coefficients are discussed in Appendices A.1 and A.2.

Substituting Eq. (44) into Eq. (42), with the help of Eq. (40) and the relations (e.g., Hagiwara, 1972; Eshagh, 2009; Šprlák et al, 2015)

$$\begin{aligned}H_n^{(p)}(\varphi, \lambda) &= \frac{2n+1}{4\pi} \int_{\psi=0}^{\pi} \int_{\lambda=0}^{2\pi} H^p(\psi, \alpha) P_{n,0}(\cos \psi) \\ &\quad \times \sin \psi d\alpha d\psi,\end{aligned}\quad (46)$$

$$\begin{aligned}\frac{\partial H_n^{(p)}(\varphi, \lambda)}{\partial \varphi} &= \frac{2n+1}{4\pi} \int_{\psi=0}^{\pi} \int_{\lambda=0}^{2\pi} H^p(\psi, \alpha) P_{n,1}(\cos \psi) \cos \alpha \\ &\quad \times \sin \psi d\alpha d\psi\end{aligned}\quad (47)$$

and

$$\begin{aligned}\frac{1}{\cos \varphi} \frac{\partial H_n^{(p)}(\varphi, \lambda)}{\partial \lambda} &= \frac{2n+1}{4\pi} \int_{\psi=0}^{\pi} \int_{\lambda=0}^{2\pi} H^p(\psi, \alpha) P_{n,1}(\cos \psi) \\ &\quad \times \sin \alpha \sin \psi d\alpha d\psi,\end{aligned}\quad (48)$$

we get

$$V^{x,\text{In}}(r, \varphi, \lambda) = -2\pi G\rho R^2 \sum_{p=1}^{\infty} \sum_{n=1}^{\infty} Q_{np}^{1,1,\text{In}}(r, \psi_0) \times \frac{\partial H_n^{(p)}(\varphi, \lambda)}{\partial \varphi}, \quad (49)$$

$$V^{y,\text{In}}(r, \varphi, \lambda) = \frac{2\pi G\rho R^2}{\cos \varphi} \sum_{p=1}^{\infty} \sum_{n=1}^{\infty} Q_{np}^{1,1,\text{In}}(r, \psi_0) \times \frac{\partial H_n^{(p)}(\varphi, \lambda)}{\partial \lambda}, \quad (50)$$

$$V^{z,\text{In}}(r, \varphi, \lambda) = 2\pi G\rho R^2 \sum_{p=1}^{\infty} \sum_{n=0}^{\infty} Q_{np}^{1,0,\text{In}}(r, \psi_0) \times H_n^{(p)}(\varphi, \lambda). \quad (51)$$

The sought Eqs. (9) – (11) for $j = \text{'In'}$ are obtained from Eqs. (49) – (51) when truncating the series over p at some finite p_{\max} , then considering that

$$H_n^{(p)} = \sum_{m=-n}^n \bar{H}_{nmp} Y_{nm}(\varphi, \lambda) \quad (52)$$

and, finally, utilizing (cf. Lemma 4.1 of Freeden and Schneider, 1998)

$$H_n^{(p)}(\varphi, \lambda) = 0 \quad \text{for } n > p \times n_{\max}. \quad (53)$$

As discussed before, the far-zone effects ($j = \text{'Out'}$) can be derived by changing the integration domain to $\psi \in [\psi_0, \pi]$. Also, we note that $H_n^{(p)}(\varphi, \lambda)$ stands for the n th-degree Laplace's surface spherical harmonic function of the p th power of the topographic height function H . It must not be confused with the p th power of the n th-degree Laplace's surface spherical harmonic function. The same applies to the notation $H_n^p(\varphi, \lambda)$ of Bucha et al (2019a), though they omitted the brackets in the superscript.

For future reference, we also provide the formulae for Molodensky's truncation coefficients related to far-zone effects,

$$\begin{aligned} Q_{np}^{1,i,\text{Out}}(r, \psi_0) &= \frac{(n-i)!}{(n+i)!} \int_0^\pi K_p^{1,i,\text{Out}}(r, \psi) P_{n,i}(\cos \psi) \\ &\quad \times \sin \psi d\psi \\ &= \frac{(n-i)!}{(n+i)!} \int_{\psi_0}^\pi \mathcal{D}^{1,i} K_p(r, \psi) P_{n,i}(\cos \psi) \\ &\quad \times \sin \psi d\psi, \quad i = 0, 1, \end{aligned} \quad (54)$$

where we introduced the kernels

$$K_p^{1,i,\text{Out}}(r, \psi) = \mathcal{D}^{1,i} K_p^{\text{Out}}(r, \psi), \quad i = 0, 1, \quad (55)$$

with

$$K_p^{\text{Out}}(r, \psi) = \begin{cases} 0 & \text{for } 0 \leq \psi < \psi_0, \\ K_p(r, \psi) & \text{for } \psi_0 \leq \psi \leq \pi. \end{cases} \quad (56)$$

A.1 Spectral representation of truncation coefficients for the first-order potential derivatives in LNOF

The spectral relations for the inner-zone truncation coefficients $Q_{np}^{1,0,\text{In}}(r, \psi_0)$ and $Q_{np}^{1,1,\text{In}}(r, \psi_0)$ can be obtained from Eq. (45) and with the help of Eqs. (29) and (38). For $Q_{np}^{1,0,\text{In}}(r, \psi_0)$, we have ($n \geq 0$)

$$\begin{aligned} Q_{np}^{1,0,\text{In}}(r, \psi_0) &= -\frac{1}{R} \sum_{l=0}^{\infty} (l+1) \left(\frac{R}{r}\right)^{l+2} \frac{\prod_{r=1}^p (l+4-r)}{p! (l+3)} \\ &\quad \times \int_0^{\psi_0} P_{l,0}(\cos \psi) P_{n,0}(\cos \psi) \sin \psi d\psi, \end{aligned} \quad (57)$$

and the coefficients $Q_{np}^{1,1,\text{In}}(r, \psi_0)$ read ($n \geq 1$)

$$\begin{aligned} Q_{np}^{1,1,\text{In}}(r, \psi_0) &= -\frac{1}{n(n+1)} \frac{1}{R} \sum_{l=1}^{\infty} \left(\frac{R}{r}\right)^{l+2} \frac{\prod_{r=1}^p (l+4-r)}{p! (l+3)} \\ &\quad \times \int_0^{\psi_0} P_{l,1}(\cos \psi) P_{n,1}(\cos \psi) \sin \psi d\psi. \end{aligned} \quad (58)$$

Note that the integral in Eq. (57) can be evaluated analytically using recurrence relations (e.g., Paul, 1973; Moreaux et al, 1999). The integral in Eq. (58) with un-normalized Legendre functions can be computed analytically similarly as shown, for instance, in Pail et al (2001) or Hwang (1991) for fully normalized Legendre functions.

For the sake of brevity, the formulae for the far-zone truncation coefficients $Q_{np}^{1,0,\text{Out}}(r, \psi_0)$ and $Q_{np}^{1,1,\text{Out}}(r, \psi_0)$ are omitted here, but can be derived from Eq. (54). This yields formally similar relations as in Eqs. (57) and (58) but with the integration domain $\psi \in [\psi_0, \pi]$.

A.2 Closed forms of truncation coefficients for the first-order potential derivatives in LNOF

After generalizing Eqs. (45) and (54) to a single expression via the superscript $j = \{\text{'In'}, \text{'Out'}\}$ and considering Eq. (38), the closed form for truncation coefficients with $i = 0$ immediately reads

$$\begin{aligned} Q_{np}^{1,0,j}(r, \psi_0) &= \frac{\partial}{\partial r} \int_0^\pi K_p^j(r, \psi) P_{n,0}(\cos \psi) \sin \psi d\psi \\ &= \frac{\partial}{\partial r} Q_{np}^j(r, \psi_0), \quad n \geq 0. \end{aligned} \quad (59)$$

The newly introduced coefficients $Q_{np}^j(r, \psi_0)$ are defined in Eqs. (28) and (32) of Bucha et al (2019a), wherein spectral

and recurrence relations can be found for an arbitrary n , p and order of the radial derivative.

For $i = 1$ in Eqs. (45) and (54), we have

$$\begin{aligned} Q_{np}^{1,1,j}(r, \psi_0) &= \frac{1}{r} \left(c^j \frac{\sin \psi_0 P_{n,1}(\cos \psi_0)}{n(n+1)} K_p(r, \psi_0) \right. \\ &\quad \left. - Q_{np}^j(r, \psi_0) \right), \quad n \geq 1, \end{aligned} \quad (60)$$

with

$$c^j = \begin{cases} 1 & \text{for } j = \text{'In'}, \\ -1 & \text{for } j = \text{'Out'}. \end{cases} \quad (61)$$

Eq. (60) was obtained from Eqs. (45) and (54) using integration by parts and the relation (e.g., Hagiwara, 1972)

$$\frac{d}{d\psi} (\sin \psi P_{n,1}(\cos \psi)) = n(n+1) P_{n,0}(\cos \psi) \sin \psi. \quad (62)$$

Note that it must hold in Eq. (62) that $\psi \in [0, \pi]$, a condition which is fulfilled in our case (cf. Eqs. 45, 54).

A.3 Spectral relations for an arbitrary radial derivative of truncation coefficients related to the first-order potential derivatives in LNOF

Differentiation of Eqs. (57) and (58) with respect to r directly leads to spectral relations for the k th radial derivative, $k \geq 1$, of $Q_{np}^{1,0,\text{In}}(r, \psi_0)$ and $Q_{np}^{1,1,\text{In}}(r, \psi_0)$,

$$\begin{aligned} \frac{\partial^k Q_{np}^{1,0,\text{In}}(r, \psi_0)}{\partial r^k} &= (-1)^{k+1} \frac{1}{R^{k+1}} \sum_{l=0}^{\infty} \prod_{e=1}^{k+1} (l+e) \\ &\quad \times \left(\frac{R}{r} \right)^{l+k+2} \frac{\prod_{r=1}^p (l+4-r)}{p!(l+3)} \\ &\quad \times \int_0^{\psi_0} P_{l,0}(\cos \psi) P_{n,0}(\cos \psi) \sin \psi d\psi, \end{aligned} \quad (63)$$

$$\begin{aligned} \frac{\partial^k Q_{np}^{1,1,\text{In}}(r, \psi_0)}{\partial r^k} &= (-1)^{k+1} \frac{1}{n(n+1)} \frac{1}{R^{k+1}} \sum_{l=1}^{\infty} \prod_{e=2}^{k+1} (l+e) \\ &\quad \times \left(\frac{R}{r} \right)^{l+k+2} \frac{\prod_{r=1}^p (l+4-r)}{p!(l+3)} \\ &\quad \times \int_0^{\psi_0} P_{l,1}(\cos \psi) P_{n,1}(\cos \psi) \sin \psi d\psi, \end{aligned} \quad (64)$$

where the former relation holds for $n \geq 0$ and latter one for $n \geq 1$.

The spectral relations for the k th radial derivative of $Q_{np}^{1,0,\text{Out}}(r, \psi_0)$ and $Q_{np}^{1,1,\text{Out}}(r, \psi_0)$ are formally similar to Eqs. (63) and (64) but with the integration domain $\psi \in [\psi_0, \pi]$.

A.4 Closed forms for an arbitrary radial derivative of truncation coefficients related to the first-order potential derivatives in LNOF

Closed forms of the k th radial derivative of the truncation coefficients $Q_{np}^{1,0,j}(r, \psi_0)$ and $Q_{np}^{1,1,j}(r, \psi_0)$ can be obtained by differentiating, respectively, Eqs. (59) and (60) with respect to r . This leads to

$$\frac{\partial^k}{\partial r^k} Q_{np}^{1,0,j}(r, \psi_0) = \frac{\partial^{k+1}}{\partial r^{k+1}} Q_{np}^j(r, \psi_0), \quad n \geq 0, k \geq 0, \quad (65)$$

and

$$\begin{aligned} \frac{\partial^k}{\partial r^k} Q_{np}^{1,1,j}(r, \psi_0) &= \sum_{q=0}^k \binom{k}{q} \left((-1)^{k-q} (k-q)! \frac{1}{r^{k-q+1}} \right. \\ &\quad \times \left(c^j \frac{\sin \psi_0 P_{n,1}(\cos \psi_0)}{n(n+1)} \frac{\partial^q}{\partial r^q} K_p(r, \psi_0) \right. \\ &\quad \left. - \frac{\partial^q}{\partial r^q} Q_{np}^j(r, \psi_0) \right), \quad n \geq 1, k \geq 0. \end{aligned} \quad (66)$$

In Eq. (66), we employed the general Leibniz rule that provides a formula for an n th derivative of a product of two n -times differentiable functions. Similarly as in Appendix A.2, the derivatives $\partial^q(Q_{np}^j(r, \psi_0))/\partial r^q$ can be computed for all $q \geq 0$ using the relations from Bucha et al (2019a). The last missing expressions are those for the radial derivatives of $K_p(r, \psi_0)$. The closed spatial relations for the k th radial derivative, $k \geq 0$, can be obtained from Eq. (30),

$$\begin{aligned} \frac{\partial^k}{\partial r^k} K_1(r, \psi) &= R \frac{\partial^k}{\partial r^k} \left(\frac{1}{l(r, \psi)} \right), \\ \frac{\partial^k}{\partial r^k} K_2(r, \psi) &= \frac{1}{2} \left(-(k-1) \frac{\partial^k}{\partial r^k} K_1(r, \psi) \right. \\ &\quad \left. - r \frac{\partial^{k+1}}{\partial r^{k+1}} K_1(r, \psi) \right), \\ \frac{\partial^k}{\partial r^k} K_p(r, \psi) &= \frac{1}{p!} \sum_{s=1}^{p-2} a_{ps} \sum_{q=0}^k \binom{k}{q} R_{p-s}^{(k-q)}(r) \\ &\quad \times \frac{\partial^{p-s+q}}{\partial r^{p-s+q}} K_1(r, \psi), \quad p \geq 3, \end{aligned} \quad (67)$$

where (Martinec, 1998)

$$\frac{\partial^k}{\partial r^k} \left(\frac{1}{l(r, \psi)} \right) = \begin{cases} \frac{1}{l(r, \psi)}, & k = 0, \\ \sum_{t=0}^k (-1)^{\frac{k+t}{2}} & \text{if } (k+t) \text{ is even} \\ \times \frac{(k-t+1)!!(k+t-1)!!}{(k-t+1)!} \frac{k!}{t!} & \\ \times \frac{(r-R \cos \psi)^t}{l^{k+t+1}(r, \psi)}, & k \geq 1, \end{cases} \quad (68)$$

and

$$R_w^{(q)}(r) = \frac{d^q}{dr^q} r^w = \begin{cases} r^w, & q = 0, w \geq 1, \\ \prod_{j=1}^q (w-j+1) r^{w-q}, & q \geq 1, w \geq 1. \end{cases} \quad (69)$$

The spectral relations for $\partial^k(K_p(r, \psi_0))/\partial r^k$ were derived by differentiating Eq. (29) with respect to r ,

$$\begin{aligned} \frac{\partial^k K_p(r, \psi)}{\partial r^k} &= \frac{(-1)^k}{R^k} \sum_{n=0}^{\infty} \prod_{l=1}^k (n+l) \left(\frac{R}{r} \right)^{n+k+1} \\ &\times \frac{\prod_{r=1}^p (n+4-r)}{p!(n+3)} P_{n,0}(\cos \psi), \quad k \geq 1. \end{aligned} \quad (70)$$

B Derivation of the second-order potential derivatives in LNOF for cap-modified spectral gravity forward modelling

In this appendix, we derive Eqs. (13) – (23) to compute the second-order derivatives of the topographic gravitational potential in LNOF. The derivation closely follows the ideas of Appendix A as well as that of Šprlák et al (2015). Therefore, they are limited to the most important steps for the sake of brevity.

First, we rewrite the differential operators from Eqs. (10) and (11) of Šprlák et al (2015) in terms of spherical polar coordinates (r, ψ, α) ,

$$\begin{aligned} \mathcal{D}^{xx} &= -\frac{1}{2} \mathcal{D}^{2,0} + \cos 2\alpha \mathcal{D}^{2,2}, \\ \mathcal{D}^{xy} &= -\sin 2\alpha \mathcal{D}^{2,2}, \\ \mathcal{D}^{xz} &= \cos \alpha \mathcal{D}^{2,1}, \\ \mathcal{D}^{yy} &= -\frac{1}{2} \mathcal{D}^{2,0} - \cos 2\alpha \mathcal{D}^{2,2}, \\ \mathcal{D}^{yz} &= -\sin \alpha \mathcal{D}^{2,1}, \\ \mathcal{D}^{zz} &= \mathcal{D}^{2,0}, \end{aligned} \quad (71)$$

where

$$\begin{aligned} \mathcal{D}^{2,0} &= \frac{\partial^2}{\partial r^2}, \\ \mathcal{D}^{2,1} &= \frac{\partial^2}{\partial r \partial \psi} \left(-\frac{1}{r} \cdot \right) = -\sin \psi \frac{\partial^2}{\partial r \partial \cos \psi} \left(-\frac{1}{r} \cdot \right), \\ \mathcal{D}^{2,2} &= \frac{1}{2r^2} \left(\frac{\partial^2}{\partial \psi^2} - \cot \psi \frac{\partial}{\partial \psi} \right) = \frac{1}{2r^2} \sin^2 \psi \frac{\partial^2}{\partial (\cos \psi)^2}. \end{aligned} \quad (72)$$

The notation $\left(-\frac{1}{r} \cdot \right)$ stands for the multiplication of the term $-\frac{1}{r}$ and the integral kernels. Again, it is presupposed that the differential operators from Eqs. (71) and (72) will only be applied to isotropic kernels having the form of Eq. (39). After applying the differential operators from Eq. (71) to Eq. (35), we get

$$\begin{aligned} V^{uv,\text{In}}(r, \phi, \lambda) &= G\rho R^2 \sum_{p=1}^{\infty} \int_{\psi=0}^{\pi} \int_{\alpha=0}^{2\pi} H^p(\psi, \alpha) K_p^{uv,\text{In}}(r, \psi) \\ &\times \sin \psi d\alpha d\psi, \quad u, v = \{x, y, z\}, \end{aligned} \quad (73)$$

where we introduced integral kernels

$$K_p^{uv,\text{In}}(r, \psi) = \mathcal{D}^{uv} K_p^{\text{In}}(r, \psi), \quad u, v = \{x, y, z\}, \quad (74)$$

which have the form

$$\begin{aligned} K_p^{xx,\text{In}} &= -\frac{1}{2} K_p^{2,0,\text{In}}(r, \psi) + \cos 2\alpha K_p^{2,2,\text{In}}(r, \psi), \\ K_p^{xy,\text{In}} &= -\sin 2\alpha K_p^{2,2,\text{In}}(r, \psi), \\ K_p^{xz,\text{In}} &= \cos \alpha K_p^{2,1,\text{In}}(r, \psi), \\ K_p^{yy,\text{In}} &= -\frac{1}{2} K_p^{2,0,\text{In}}(r, \psi) - \cos 2\alpha K_p^{2,2,\text{In}}(r, \psi), \\ K_p^{yz,\text{In}} &= -\sin \alpha K_p^{2,1,\text{In}}(r, \psi), \\ K_p^{zz,\text{In}} &= K_p^{2,0,\text{In}}(r, \psi), \end{aligned} \quad (75)$$

with

$$K_p^{2,i,\text{In}}(r, \psi) = \mathcal{D}^{2,i} K_p^{\text{In}}(r, \psi), \quad i = 0, 1, 2. \quad (76)$$

Next, the kernels from Eq. (76) are expanded in series of un-normalized Legendre functions as

$$K_p^{2,i,\text{In}}(r, \psi) = \sum_{n=i}^{\infty} \frac{2n+1}{2} Q_{np}^{2,i,\text{In}}(r, \psi_0) P_{n,i}(\cos \psi) \quad (77)$$

with $i = 0, 1, 2$ and Molodensky's truncation coefficients $Q_{np}^{2,i,\text{In}}(r, \psi_0)$ defined as

$$\begin{aligned} Q_{np}^{2,i,\text{In}}(r, \psi_0) &= \frac{(n-i)!}{(n+i)!} \int_0^{\pi} K_p^{2,i,\text{In}}(r, \psi) P_{n,i}(\cos \psi) \sin \psi d\psi \\ &= \frac{(n-i)!}{(n+i)!} \int_0^{\psi_0} \mathcal{D}^{2,i} K_p(r, \psi) P_{n,i}(\cos \psi) \sin \psi d\psi. \end{aligned}$$

(78)

Numerical evaluation of these coefficients via spectral and closed spatial relations is discussed in Appendices B.1 and B.2, respectively.

With the help of Eqs. (78), (77), (76), (75) and (73) of this paper as well as using Eqs. (47) and (48) of Šprlák et al (2015), we arrive at the expressions

$$\begin{aligned} V^{xx,\text{In}}(r, \varphi, \lambda) &= 2\pi G\rho R^2 \\ &\times \sum_{p=1}^{\infty} \sum_{n=0}^{\infty} \left[-\frac{1}{2} Q_{np}^{2,0,\text{In}}(r, \psi_0) H_n^{(p)}(\varphi, \lambda) \right. \\ &+ Q_{np}^{2,2,\text{In}}(r, \psi_0) \left(n(n+1) H_n^{(p)}(\varphi, \lambda) \right. \\ &\left. \left. + 2 \frac{\partial^2 H_n^{(p)}(\varphi, \lambda)}{\partial \varphi^2} \right) \right], \end{aligned} \quad (79)$$

$$\begin{aligned} V^{xy,\text{In}}(r, \varphi, \lambda) &= -\frac{2\pi G\rho R^2}{\cos \varphi} \sum_{p=1}^{\infty} \sum_{n=0}^{\infty} Q_{np}^{2,2,\text{In}}(r, \psi_0) \\ &\times 2 \left(\tan \varphi \frac{\partial H_n^{(p)}(\varphi, \lambda)}{\partial \lambda} + \frac{\partial^2 H_n^{(p)}(\varphi, \lambda)}{\partial \lambda \partial \varphi} \right), \end{aligned} \quad (80)$$

$$\begin{aligned} V^{xz,\text{In}}(r, \varphi, \lambda) &= 2\pi G\rho R^2 \sum_{p=1}^{\infty} \sum_{n=0}^{\infty} Q_{np}^{2,1,\text{In}}(r, \psi_0) \\ &\times \frac{\partial H_n^{(p)}(\varphi, \lambda)}{\partial \varphi}, \end{aligned} \quad (81)$$

$$\begin{aligned} V^{yy,\text{In}}(r, \varphi, \lambda) &= 2\pi G\rho R^2 \\ &\times \sum_{p=1}^{\infty} \sum_{n=0}^{\infty} \left[-\frac{1}{2} Q_{np}^{2,0,\text{In}}(r, \psi_0) H_n^{(p)}(\varphi, \lambda) \right. \\ &- Q_{np}^{2,2,\text{In}}(r, \psi_0) \left(n(n+1) H_n^{(p)}(\varphi, \lambda) \right. \\ &\left. \left. + 2 \frac{\partial^2 H_n^{(p)}(\varphi, \lambda)}{\partial \varphi^2} \right) \right], \end{aligned} \quad (82)$$

$$\begin{aligned} V^{yz,\text{In}}(r, \varphi, \lambda) &= -\frac{2\pi G\rho R^2}{\cos \varphi} \sum_{p=1}^{\infty} \sum_{n=0}^{\infty} Q_{np}^{2,1,\text{In}}(r, \psi_0) \\ &\times \frac{\partial H_n^{(p)}(\varphi, \lambda)}{\partial \lambda}, \end{aligned} \quad (83)$$

$$\begin{aligned} V^{zz,\text{In}}(r, \varphi, \lambda) &= 2\pi G\rho R^2 \sum_{p=1}^{\infty} \sum_{n=0}^{\infty} Q_{np}^{2,0,\text{In}}(r, \psi_0) \\ &\times H_n^{(p)}(\varphi, \lambda). \end{aligned} \quad (84)$$

Note that the non-existing coefficients $Q_{0p}^{2,1,\text{In}}(r, \psi_0)$, $Q_{0p}^{2,2,\text{In}}(r, \psi_0)$, and $Q_{1p}^{2,2,\text{In}}(r, \psi_0)$ are set to zero in Eqs. (79) – (84).

Finally, after truncating the series over p at some finite p_{\max} and considering Eqs. (52) and (53), we obtain Eqs. (13) – (23) for $j = \text{'In'}$.

The relations for $j = \text{'Out'}$ can similarly be derived by changing the integration domain to $\psi \in [\psi_0, \pi]$ which requires to introduce the truncation coefficients

$$\begin{aligned} Q_{np}^{2,i,\text{Out}}(r, \psi_0) &= \frac{(n-i)!}{(n+i)!} \int_0^\pi K_p^{2,i,\text{Out}}(r, \psi) P_{n,i}(\cos \psi) \\ &\times \sin \psi d\psi \\ &= \frac{(n-i)!}{(n+i)!} \int_{\psi_0}^\pi \mathcal{D}^{2,i} K_p(r, \psi) P_{n,i}(\cos \psi) \\ &\times \sin \psi d\psi, \quad i = 0, 1, 2, \end{aligned} \quad (85)$$

with

$$K_p^{2,i,\text{Out}}(r, \psi) = \mathcal{D}^{2,i} K_p^{\text{Out}}(r, \psi), \quad i = 0, 1, 2. \quad (86)$$

B.1 Spectral representation of truncation coefficients for the second-order potential derivatives in LNOF

The inner-zone truncation coefficients expressed in the spectral form read

$$\begin{aligned} Q_{np}^{2,0,\text{In}}(r, \psi_0) &= \frac{1}{R^2} \sum_{l=0}^{\infty} (l+1)(l+2) \left(\frac{R}{r} \right)^{l+3} \frac{\prod_{r=1}^p (l+4-r)}{p! (l+3)} \\ &\times \int_0^{\psi_0} P_{l,0}(\cos \psi) P_{n,0}(\cos \psi) \sin \psi d\psi, \end{aligned} \quad (87)$$

$$\begin{aligned} Q_{np}^{2,1,\text{In}}(r, \psi_0) &= -\frac{1}{(n+1)n} \frac{1}{R^2} \sum_{l=1}^{\infty} (l+2) \left(\frac{R}{r} \right)^{l+3} \\ &\times \frac{\prod_{r=1}^p (l+4-r)}{p! (l+3)} \\ &\times \int_0^{\psi_0} P_{l,1}(\cos \psi) P_{n,1}(\cos \psi) \sin \psi d\psi \end{aligned} \quad (88)$$

and

$$\begin{aligned} Q_{np}^{2,2,\text{In}}(r, \psi_0) &= \frac{1}{(n+2)(n+1)n(n-1)} \frac{1}{2R^2} \\ &\times \sum_{l=2}^{\infty} \left(\frac{R}{r}\right)^{l+3} \prod_{r=1}^p (l+4-r) \\ &\times \int_0^{\psi_0} P_{l,2}(\cos \psi) P_{n,2}(\cos \psi) \sin \psi d\psi, \end{aligned} \quad (89)$$

for $n \geq 0$, $n \geq 1$ and $n \geq 2$, respectively. These equations were derived from Eq. (78) using Eqs. (29) and (72). The far-zone coefficients can be derived in a similar manner from Eq. (85), see also Appendix A.1. Note that the integrals in Eqs. (87) – (89) can be evaluated analytically (cf. Appendix A.1).

B.2 Closed forms of truncation coefficients for the second-order potential derivatives in LNOF

Considering Eq. (72), the closed form of truncation coefficients for the second-order potential derivatives (Eqs. 78 and 85) reads for $i = 0$ ($n \geq 0$)

$$Q_{np}^{2,0,j}(r, \psi_0) = \frac{\partial Q_{np}^{1,0,j}(r, \psi_0)}{\partial r} = \frac{\partial^2 Q_{np}^j(r, \psi_0)}{\partial r^2}. \quad (90)$$

For $i = 1$, we have the relation ($n \geq 1$)

$$\begin{aligned} Q_{np}^{2,1,j}(r, \psi_0) &= \frac{1}{r} \left[c^j \frac{\sin \psi_0 P_{n,1}(\cos \psi_0)}{n(n+1)} \right. \\ &\times \left(\frac{1}{r} K_p(r, \psi_0) - \frac{\partial}{\partial r} K_p(r, \psi_0) \right) \\ &- \left. \left(\frac{1}{r} Q_{np}^j(r, \psi_0) - \frac{\partial}{\partial r} Q_{np}^j(r, \psi_0) \right) \right] \\ &= \frac{1}{r} \left(Q_{np}^{1,1,j}(r, \psi_0) - \frac{\partial}{\partial r} (r Q_{np}^{1,1,j}(r, \psi_0)) \right), \end{aligned} \quad (91)$$

where we employed integration by parts together with Eq. (62).

Finally, the formula for $i = 2$ reads ($n \geq 2$)

$$\begin{aligned} Q_{np}^{2,2,j}(r, \psi_0) &= \frac{1}{2r^2} \left(c^j \frac{\sin \psi_0 P_{n,2}(\cos \psi_0)}{(n+2)(n+1)n(n-1)} \frac{\partial K_p(r, \psi_0)}{\partial \psi} \right. \\ &- c^j \frac{\sin \psi_0 P_{n,1}(\cos \psi_0)}{n(n+1)} K_p(r, \psi_0) \\ &\left. + Q_{np}^j(r, \psi_0) \right). \end{aligned} \quad (92)$$

This equation was derived by applying integration by parts twice, utilizing Eq. (62) and the recurrence relation (e.g.,

Freeden and Schreiner, 2009)

$$\begin{aligned} \sin^2 \psi \frac{dP_{n,m}(\cos \psi)}{d \cos \psi} - m \cos \psi P_{n,m}(\cos \psi) \\ = -(n+m)(n-m+1) \sin \psi P_{n,m-1}(\cos \psi). \end{aligned} \quad (93)$$

Again, we acknowledge that ψ must be from the interval $[0, \pi]$ in this equation which is satisfied in our case.

B.3 Spectral relations for an arbitrary radial derivative of truncation coefficients related to the second-order potential derivatives in LNOF

The spectral form of the k th radial derivative of the inner-zone truncation coefficients related to the second-order potential derivatives can be obtained by differentiating k times ($k \geq 1$) Eqs. (87) – (89) with respect to r and read

$$\begin{aligned} \frac{\partial^k Q_{np}^{2,0,\text{In}}(r, \psi_0)}{\partial r^k} &= (-1)^k \frac{1}{R^{k+2}} \sum_{l=0}^{\infty} \prod_{e=1}^{k+2} (l+e) \left(\frac{R}{r}\right)^{l+k+3} \\ &\times \prod_{r=1}^p (l+4-r) \\ &\times \int_0^{\psi_0} P_{l,0}(\cos \psi) P_{n,0}(\cos \psi) \sin \psi d\psi, \end{aligned} \quad (94)$$

$$\begin{aligned} \frac{\partial^k Q_{np}^{2,1,\text{In}}(r, \psi_0)}{\partial r^k} &= (-1)^{k+1} \frac{1}{(n+1)n} \frac{1}{R^{k+2}} \sum_{l=1}^{\infty} \prod_{e=2}^{k+2} (l+e) \\ &\times \left(\frac{R}{r}\right)^{l+k+3} \prod_{r=1}^p (l+4-r) \\ &\times \int_0^{\psi_0} P_{l,1}(\cos \psi) P_{n,1}(\cos \psi) \sin \psi d\psi \end{aligned} \quad (95)$$

and

$$\begin{aligned} \frac{\partial^k Q_{np}^{2,2,\text{In}}(r, \psi_0)}{\partial r^k} &= (-1)^k \frac{1}{(n+2)(n+1)n(n-1)} \frac{1}{2R^{k+2}} \\ &\times \sum_{l=2}^{\infty} \prod_{e=3}^{k+2} (l+e) \left(\frac{R}{r}\right)^{l+k+3} \\ &\times \prod_{r=1}^p (l+4-r) \\ &\times \int_0^{\psi_0} P_{l,2}(\cos \psi) P_{n,2}(\cos \psi) \sin \psi d\psi \end{aligned}$$

for $n \geq 0$, $n \geq 1$ and $n \geq 2$, respectively.

Formally similar equations hold also for the far-zone coefficients, but with the integration domain being $\psi \in [\psi_0, \pi]$.

B.4 Closed forms for an arbitrary radial derivative of truncation coefficients related to the second-order potential derivatives in LNOF

The closed form of the k th radial derivative of the truncation coefficients $Q_{np}^{2,0,j}(r, \psi_0)$ from Eq. (90) reads

$$\frac{\partial^k}{\partial r^k} Q_{np}^{2,0,j}(r, \psi_0) = \frac{\partial^{k+2} Q_{np}^j(r, \psi_0)}{\partial r^{k+2}}, \quad n \geq 0, k \geq 0, \quad (97)$$

where the spectral and recurrence relations for $Q_{np}^j(r, \psi_0)$ and its derivatives can be found in Bucha et al (2019a).

Applying the general Leibniz rule, we get for $Q_{np}^{2,1,j}(r, \psi_0)$ from Eq. (91) the relation

$$\begin{aligned} \frac{\partial^k}{\partial r^k} Q_{np}^{2,1,j}(r, \psi_0) &= \sum_{q=0}^k \binom{k}{q} \left((-1)^{k-q} (k-q)! \frac{1}{r^{k-q+1}} \right) \\ &\times \left(\frac{\partial^q}{\partial r^q} Q_{np}^{1,1,j}(r, \psi_0) \right. \\ &- c^j \frac{\sin \psi_0 P_{n,1}(\cos \psi_0)}{n(n+1)} \frac{\partial^{q+1}}{\partial r^{q+1}} K_p(r, \psi_0) \\ &\left. + \frac{\partial^{q+1}}{\partial r^{q+1}} Q_{np}^j(r, \psi_0) \right), \quad n \geq 1, k \geq 0. \end{aligned} \quad (98)$$

Finally, differentiating Eq. (92) leads to

$$\begin{aligned} \frac{\partial^k}{\partial r^k} Q_{np}^{2,2,j}(r, \psi_0) &= \frac{1}{2} \sum_{q=0}^k \binom{k}{q} \\ &\times \left((-1)^{k-q} (k-q+1)! \frac{1}{r^{k-q+2}} \right) \\ &\times \left(c^j \frac{\sin \psi_0 P_{n,2}(\cos \psi_0)}{(n+2)(n+1)n(n-1)} \right. \\ &\times \frac{\frac{\partial^{q+1}}{\partial r^q} K_p(r, \psi_0) - c^j \sin \psi_0 P_{n,1}(\cos \psi_0)}{n(n+1)} \\ &\left. \times \frac{\partial^q}{\partial r^q} K_p(r, \psi_0) + \frac{\partial^q}{\partial r^q} Q_{np}^j(r, \psi_0) \right) \end{aligned} \quad (99)$$

for all $n \geq 2$ and $k \geq 0$.

The derivatives of $K_p(r, \psi_0)$ with respect to r and ψ from Eq. (99) can be obtained by differentiating Eqs. (67) and

(96)

(70) with respect to ψ . For $k \geq 0$, the closed spatial relations read

$$\begin{aligned} \frac{\partial^{k+1}}{\partial r^k \partial \psi} K_1(r, \psi) &= R \frac{\partial^{k+1}}{\partial r^k \partial \psi} \left(\frac{1}{l(r, \psi)} \right), \\ \frac{\partial^{k+1}}{\partial r^k \partial \psi} K_2(r, \psi) &= \frac{1}{2} \left(-(k-1) \frac{\partial^{k+1}}{\partial r^k \partial \psi} K_1(r, \psi) \right. \\ &\left. - r \frac{\partial^{k+2}}{\partial r^{k+1} \partial \psi} K_1(r, \psi) \right), \end{aligned} \quad (100)$$

$$\begin{aligned} \frac{\partial^{k+1}}{\partial r^k \partial \psi} K_p(r, \psi) &= \frac{1}{p!} \sum_{s=1}^{p-2} a_{ps} \sum_{q=0}^k \binom{k}{q} R_{p-s}^{(k-q)}(r) \\ &\times \frac{\partial^{p-s+q+1}}{\partial r^{p-s+q} \partial \psi} K_1(r, \psi), \quad p \geq 3, \end{aligned}$$

with

$$\begin{aligned} \frac{\partial^{k+1}}{\partial r^k \partial \psi} \left(\frac{1}{l(r, \psi)} \right) &= \frac{\partial^{k+1}}{\partial \psi \partial r^k} \left(\frac{1}{l(r, \psi)} \right) \\ &= \begin{cases} -\frac{rR \sin \psi}{l^3(r, \psi)}, & k=0, \\ \sum_{\substack{(k+t) \text{ is even} \\ t=0}}^k (-1)^{\frac{k+t}{2}} \\ \times \frac{(k-t+1)!!(k+t-1)!!}{(k-t+1)!} \frac{k!}{t!} \\ \times \left[\frac{(r-R \cos \psi)^{t-1} R \sin \psi}{l^{k+t+1}(r, \psi)} \right. \\ \left. \times \left(t - (r-R \cos \psi)r \frac{k+t+1}{l^2(r, \psi)} \right) \right], & k \geq 1. \end{cases} \end{aligned} \quad (101)$$

Eq. (101) was derived from Eq. (68). Finally, the spectral counterpart of Eq. (100) was derived from Eqs. (29) and (70), and read

$$\frac{\partial K_p(r, \psi)}{\partial \psi} = - \sum_{n=1}^{\infty} \left(\frac{R}{r} \right)^{n+1} \frac{\prod_{r=1}^p (n+4-r)}{p!(n+3)} P_{n,1}(\cos \psi) \quad (102)$$

for $k=0$ and

$$\begin{aligned} \frac{\partial^{k+1} K_p(r, \psi)}{\partial r^k \partial \psi} &= \frac{(-1)^{k+1}}{R^k} \sum_{n=1}^{\infty} \prod_{e=1}^k (n+e) \left(\frac{R}{r} \right)^{n+k+1} \\ &\times \frac{\prod_{r=1}^p (n+4-r)}{p!(n+3)} P_{n,1}(\cos \psi) \end{aligned} \quad (103)$$

for $k \geq 1$.

C Indirect check on the numerical accuracy of evaluated truncation coefficients

The numerical accuracy of evaluated truncation coefficients $Q_{np}^{\text{In}}(r, \psi_0)$ and $Q_{np}^{\text{Out}}(r, \psi_0)$ (cf. Eq. 6) can be checked indirectly through the identity (Bucha et al, 2019a)

$$Q_{np}^{\text{In}}(r, \psi_0) + Q_{np}^{\text{Out}}(r, \psi_0) = S_{np}(r). \quad (104)$$

Translated into gravity effects, when adding near- and far-zone gravity effects (equivalent to the left-hand side of the equation), the result must be identical to the global gravity effect (the right-hand side of the equation) from global spectral modelling (cf. Section 2 of this paper and also Section 3 of Bucha et al 2019a).

For the k th radial derivative, $k \geq 1$, we have

$$\frac{\partial^k Q_{np}^{\text{In}}(r, \psi_0)}{\partial r^k} + \frac{\partial^k Q_{np}^{\text{Out}}(r, \psi_0)}{\partial r^k} = \frac{\partial^k S_{np}(r)}{\partial r^k}, \quad (105)$$

where

$$\begin{aligned} \frac{\partial^k S_{np}(r)}{\partial r^k} &= \frac{(-1)^k}{R^k} \frac{2}{2n+1} \frac{\prod_{i=1}^p (n+4-i)}{p!(n+3)} \\ &\times \prod_{e=1}^k (n+e) \left(\frac{R}{r}\right)^{n+k+1}, \quad k \geq 1, \end{aligned} \quad (106)$$

and the relations for the radial derivatives of $Q_{np}^{\text{In}}(r, \psi_0)$ and $Q_{np}^{\text{Out}}(r, \psi_0)$ were discussed in Bucha et al (2019a). Eq. (105) can also be used to check the numerical accuracy of $Q_{np}^{1,0,j}(r, \psi_0)$ and $Q_{np}^{2,0,j}(r, \psi_0)$ (see Eqs. 59 and 90, respectively).

For the newly derived coefficients $Q_{np}^{1,1,j}(r, \psi_0)$, $Q_{np}^{2,1,j}(r, \psi_0)$, $Q_{np}^{2,2,j}(r, \psi_0)$ and their radial derivatives, the following relations can be derived from Eqs. (58), (88), (89), (64), (95) and (96) when exploiting the orthogonality of Legendre functions,

$$\begin{aligned} \frac{\partial^k Q_{np}^{1,1,\text{In}}(r, \psi_0)}{\partial r^k} + \frac{\partial^k Q_{np}^{1,1,\text{Out}}(r, \psi_0)}{\partial r^k} \\ = \begin{cases} -\frac{1}{R} \frac{2}{2n+1} \left(\frac{R}{r}\right)^{n+2} \frac{\prod_{r=1}^p (n+4-r)}{p!(n+3)}, & k=0, \\ \frac{(-1)^{k+1}}{R^{k+1}} \frac{2}{2n+1} \prod_{e=2}^{k+1} (n+e) \left(\frac{R}{r}\right)^{n+k+2} \\ \times \frac{\prod_{r=1}^p (n+4-r)}{p!(n+3)}, & k \geq 1, \end{cases} \end{aligned} \quad (107)$$

$$\begin{aligned} &\frac{\partial^k Q_{np}^{2,1,\text{In}}(r, \psi_0)}{\partial r^k} + \frac{\partial^k Q_{np}^{2,1,\text{Out}}(r, \psi_0)}{\partial r^k} \\ &= \frac{(-1)^{k+1}}{R^{k+2}} \frac{2}{2n+1} \prod_{e=2}^{k+2} (n+e) \left(\frac{R}{r}\right)^{n+k+3} \\ &\times \frac{\prod_{r=1}^p (n+4-r)}{p!(n+3)}, \quad k \geq 0, \end{aligned} \quad (108)$$

$$\begin{aligned} &\frac{\partial^k Q_{np}^{2,2,\text{In}}(r, \psi_0)}{\partial r^k} + \frac{\partial^k Q_{np}^{2,2,\text{Out}}(r, \psi_0)}{\partial r^k} \\ &= \begin{cases} \frac{1}{2R^2} \frac{2}{2n+1} \left(\frac{R}{r}\right)^{n+3} \frac{\prod_{r=1}^p (n+4-r)}{p!(n+3)}, & k=0, \\ \frac{(-1)^k}{2R^{k+2}} \frac{2}{2n+1} \prod_{e=3}^{k+2} (n+e) \left(\frac{R}{r}\right)^{n+k+3} \\ \times \frac{\prod_{r=1}^p (n+4-r)}{p!(n+3)}, & k \geq 1. \end{cases} \end{aligned} \quad (109)$$

In Eqs. (107), (108) and (109), it must be satisfied that $n \geq 1$, $n \geq 1$ and $n \geq 2$, respectively (cf. Eqs. 64, 95 and 96).

Note that this validation method is indirect only, because all these equations compare the sums of near- and far-zone truncation coefficients instead of validating directly the individual coefficients. However, as mentioned by Bucha et al (2019a), a direct validation does not seem to be possible at the present time, given that no relations for the truncation coefficients are known to the authors beside those in Bucha et al (2019a) and this paper.

References

- Balmino G (1994) Gravitational potential harmonics from the shape of an homogeneous body. *Celestial Mechanics and Dynamical Astronomy* 60:331–364
- Balmino G, Vales N, Bonvalot S, Briais A (2012) Spherical harmonic modelling to ultra-high degree of Bouguer and isostatic anomalies. *Journal of Geodesy* 86:499–520, doi: 10.1007/s00190-011-0533-4
- Bucha B, Janák J (2013) A MATLAB-based graphical user interface program for computing functionals of the geopotential up to ultra-high degrees and orders. *Computers and Geosciences* 56:186–196, doi: 10.1016/j.cageo.2013.03.012

- Bucha B, Janák J (2014) A MATLAB-based graphical user interface program for computing functionals of the geopotential up to ultra-high degrees and orders: Efficient computation at irregular surfaces. *Computers and Geosciences* 66:219–227, doi: 10.1016/j.cageo.2014.02.005
- Bucha B, Janák J, Papčo J, Bezděk A (2016) High-resolution regional gravity field modelling in a mountainous area from terrestrial gravity data. *Geophysical Journal International* 207:949–966, doi: 10.1093/gji/ggw311
- Bucha B, Hirt C, Kuhn M (2019a) Cap integration in spectral gravity forward modelling: near- and far-zone gravity effects via Molodensky's truncation coefficients. *Journal of Geodesy* 93:65–83, doi: 10.1007/s00190-018-1139-x
- Bucha B, Hirt C, Kuhn M (2019b) Divergence-free spherical harmonic gravity field modelling based on the Runge-Krarup theorem: a case study for the Moon. *Journal of Geodesy* 93:489–513, doi: 10.1007/s00190-018-1177-4
- Chen C, Ouyang Y, Blan S (2019) Spherical harmonic expansions for the gravitational field of a polyhedral body with polynomial density contrast. *Surveys in Geophysics* doi: 10.1007/s10712-019-09515-1
- Eshagh M (2009) On satellite gravity gradiometry. PhD thesis, Royal Institute of Technology, Division of Geodesy, Stockholm, Sweden, 222 pp
- Freedon W, Gerhards C (2013) Geomathematically Oriented Potential Theory. CRC Press, Boca Raton, Fl, 447 pp
- Freedon W, Schneider F (1998) Wavelet approximations on closed surfaces and their application to boundary-value problems of potential theory. *Mathematical Methods in the Applied Sciences* 21:129–163
- Freedon W, Schreiner M (2009) Spherical Functions of Mathematical Geosciences: A Scalar, Vectorial, and Tensorial Setup. Springer-Verlag, Berlin Heidelberg, 602 pp
- Fukushima T (2012) Numerical computation of spherical harmonics of arbitrary degree and order by extending exponent of floating point numbers. *Journal of Geodesy* 86:271–285, doi: 10.1007/s00190-011-0519-2
- Garmier R, Barriot JP (2001) Ellipsoidal harmonic expansions of the gravitational potential: Theory and applications. *Celestial Mechanics and Dynamical Astronomy* 79:235–275
- Gradshteyn IS, Ryzhik IM (2007) Table of Integrals, Series, and Products, seventh edn. Academic Press, 1172 pp
- Grombein T, Seitz K, Heck B (2013) Optimized formulas for the gravitational field of a tesseroid. *Journal of Geodesy* 87:645–660, doi: 10.1007/s00190-013-0636-1
- Hagiwara Y (1972) Truncation error formulas for the geoidal height and the deflection of the vertical. *Bulletin Géodésique* 46:453–466, doi: 10.1007/BF02522052
- Heiskanen WA, Moritz H (1967) Physical Geodesy. W. H. Freeman and Company, San Francisco, 364 pp
- Hirt C (2012) Efficient and accurate high-degree spherical harmonic synthesis of gravity field functionals at the Earth's surface using the gradient approach. *Journal of Geodesy* 86:729–744, doi: 10.1007/s00190-012-0550-y
- Hirt C, Kuhn M (2014) Band-limited topographic mass distribution generates full-spectrum gravity field: Gravity forward modeling in the spectral and spatial domains revisited. *Journal of Geophysical Research: Solid Earth* 119:3646–3661, doi: 10.1002/2013JB010900
- Hirt C, Kuhn M (2017) Convergence and divergence in spherical harmonic series of the gravitational field generated by high-resolution planetary topography—A case study for the Moon. *Journal of Geophysical Research: Planets* 122:1727–1746, doi: 10.1002/2017JE005298
- Hirt C, Rexer M (2015) Earth2014: 1 arc-min shape, topography, bedrock and ice-sheet models available as gridded data and degree-10,800 spherical harmonics. *International Journal of Applied Earth Observation and Geoinformation* 39:103–112, doi: 10.1016/j.jag.2015.03.001
- Hirt C, Reußner E, Rexer M, Kuhn M (2016) Topographic gravity modeling for global Bouguer maps to degree 2160: Validation of spectral and spatial domain forward modeling techniques at the 10 microgal level. *Journal of Geophysical Research: Solid Earth* 121:6846–6862, doi: 10.1002/2016JB013249
- Hirt C, Bucha B, Yang M, Kuhn M (2019) A numerical study of residual terrain modelling (RTM) techniques and the harmonic correction using ultra-high degree spectral gravity modelling. *Journal of Geodesy* doi: 10.1007/s00190-019-01261-x
- Holmes SA (2003) High degree spherical harmonic synthesis for simulated earth gravity modelling. PhD thesis, Department of Spatial Sciences, Curtin University of Technology, Perth, Australia, 171 pp
- Hotine M (1969) Mathematical Geodesy. U.S. Department of Commerce, Washington, D.C., 416 pp
- Hu X, Jekeli C (2015) A numerical comparison of spherical, spheroidal and ellipsoidal harmonic gravitational field models for small non-spherical bodies: examples for the Martian moons. *Journal of Geodesy* 89:159–177, doi: 10.1007/s00190-014-0769-x
- Hwang C (1991) Orthogonal functions over the oceans and applications to the determination of orbit error, geoid and sea surface topography from satellite altimetry. Report No. 414, Department of Geodetic Science and Surveying, The Ohio State University, Columbus, Ohio, 229 pp
- Jekeli C (1981) The downward continuation to the Earth's surface of truncated spherical and ellipsoidal harmonic series of the gravity and height anomalies. Report No. 11, Department of Geodetic Science and Surveying, The Ohio State University, Columbus, Ohio, 140 pp
- Jekeli C (1983) A numerical study of the divergence of spherical harmonic series of the gravity and height anomalies at the Earth's surface. *Bulletin Géodésique* 57:10–28

- Martinec Z (1998) Boundary-Value Problems for Gravimetric Determination of a Precise Geoid. Springer-Verlag, Berlin, Heidelberg, 223 pp
- Martinec Z, Pěč K (1989) The Phobos gravitational field modeled on the basis of its topography. *Earth, Moon, and Planets* 45:219–235
- Molodensky MS, Eremeev VF, Yurkina MI (1962) Methods for Study of the External Gravitational Field and Figure of the Earth. Israel Program for Scientific Translations, Jerusalem, 248 pp, translated from Russian (1960)
- Moreaux G, Tscherning CC, Sansò F (1999) Approximation of harmonic covariance functions on the sphere by non-harmonic locally supported functions. *Journal of Geodesy* 73:555–567
- Moritz H (1980) Advanced Physical Geodesy. Herbert Wichmann Verlag, Karlsruhe, Germany, 500 pp
- Moritz H (2003) The strange behavior of asymptotic series in mathematics, celestial mechanics and physical geodesy. In: Grafarend EW, Krumm FW, Schwarze VS (eds) *Geodesy: The Challenge of the Third Millennium*, Springer-Verlag, Berlin, Heidelberg, pp 371–377
- Moritz H (2010) Classical physical geodesy. In: Freedman W, Nashed MZ, Sonar T (eds) *Handbook of Geomathematics*, Springer-Verlag, Berlin, Heidelberg, pp 127–158
- Pail R, Plank G, Schuh WD (2001) Spatially restricted data distributions on the sphere: the method of orthonormalized functions and applications. *Journal of Geodesy* 75:44–56, doi: 10.1007/s001900000153
- Paul MK (1973) A method of evaluating the truncation error coefficients for geoidal height. *Bulletin Géodésique* 110:413–425
- Pavlis NK, Holmes SA, Kenyon SC, Factor JK (2012) The development and evaluation of the Earth Gravitational Model 2008 (EGM2008). *Journal of Geophysical Research* 117(B04406):1–38, doi: 10.1029/2011JB008916
- Petrovskaya MS, Vershkov AN (2006) Non-singular expressions for the gravity gradients in the local north-oriented and orbital reference frames. *Journal of Geodesy* 80:117–127, doi: 10.1007/s00190-006-0031-2
- Reimond S, Baur O (2016) Spheroidal and ellipsoidal harmonic expansions of the gravitational potential of small Solar System bodies. Case study: Comet 67P/Churyumov-Gerasimenko. *Journal of Geophysical Research: Planets* 121:497–515, doi: 10.1002/2015JE004965
- Rexer M (2017) Spectral solutions to the topographic potential in the context of high-resolution global gravity field modelling. PhD thesis, Technische Universität München, München, Germany, 212 pp
- Rexer M, Hirt C, Claessens S, Tenzer R (2016) Layer-based modelling of the Earth's gravitational potential up to 10-km scale in spherical harmonics in spherical and ellipsoidal approximation. *Surveys in Geophysics* 37:1035–1074, doi: 10.1007/s10712-016-9382-2
- Rexer M, Hirt C, Bucha B, Holmes S (2018) Solution to the spectral filter problem of residual terrain modelling (RTM). *Journal of Geodesy* 92:675–690, doi: 10.1007/s00190-017-1086-y
- Rummel R, Rapp RH, Sünkel H, Tscherning CC (1988) Comparisons of global topographic/isostatic models to the Earth's observed gravity field. Report No. 388, Department of Geodetic Science and Surveying, The Ohio State University, Columbus, Ohio, 33 pp
- Sacerdote F, Sansò F (2010) Least squares, Galerkin and BVPs applied to the determination of global gravity field models. In: Mertikas SP (ed) *Gravity, Geoid and Earth Observation: Proceedings of the IAG Commission 2: Gravity Field*, Chania, Crete, Greece, 23–27 June 2008, Springer, vol 135, pp 511–517, ISBN 978-3-642-10633-0, e-ISSN 978-3-642-10634-7
- Sansò F, Sideris MG (2013) *Geoid Determination: Theory and Methods*. Springer, Berlin, Heidelberg, 734 pp
- Sebera J, Bezděk A, Pešek I, Henych T (2016) Spheroidal models of the exterior gravitational field of asteroids Bennu and Castalia. *Icarus* 272:70–79, doi: 10.1016/j.icarus.2016.02.038
- Sjöberg L (1977) On the errors of spherical harmonic developments of gravity at the surface of the Earth. Report No. 12, Department of Geodetic Science, The Ohio State University, Columbus, Ohio, 74 pp
- Sjöberg L, Bagherbandi M (2017) *Gravity Inversion and Integration: Theory and Application in Geodesy and Geophysics*. Springer, 383 pp
- Sneeuw N (1994) Global spherical harmonic analysis by least-squares and numerical quadrature methods in historical perspective. *Geophysical Journal International* 118:707–716
- Šprlák M, Hamáčková E, Novák P (2015) Alternative validation method of satellite gradiometric data by integral transform of satellite altimetry data. *Journal of Geodesy* 89:757–773, doi: 10.1007/s00190-015-0813-5
- Takahashi Y, Scheeres DJ (2014) Small body surface gravity fields via spherical harmonic expansions. *Celestial Mechanics and Dynamical Astronomy* 119:169–206, doi: 10.1007/s10569-014-9552-9
- Tenzer R, Hirt C, Novák P, Pitoňák M, Šprlák M (2016) Contribution of mass density heterogeneities to the quasigeoid-to-geoid separation. *Journal of Geodesy* 90:65–80, doi: 10.1007/s00190-015-0858-5
- Tsoulis D (2012) Analytical computation of the full gravity tensor of a homogeneous arbitrarily shaped polyhedral source using line integrals. *Geophysics* 77:F1–F11, doi: 10.1190/GEO2010-0334.1
- Wang YM, Yang X (2013) On the spherical and spheroidal harmonic expansion of the gravitational potential of the topographic masses. *Journal of Geodesy* 87:909–921, doi:

- 10.1007/s00190-013-0654-z
- Wessel P, Smith WHF (1998) New, improved version of generic mapping tools released. EOS, Transactions American Geophysical Union 79:579, doi: 10.1029/98EO00426
- Wieczorek MA, Phillips RJ (1998) Potential anomalies on a sphere: Applications to the thickness of the lunar crust. Journal of Geophysical Research 103:1715–1724
- de Witte L (1967) Truncation errors in the Stokes and Venring Meinesz formulae for different order spherical harmonic gravity terms. Geophysical Journal of the Royal Astronomical Society 12:449–464, doi: 10.1111/j.1365-246X.1967.tb03125.x